Vertical confinement effects on a fully developed turbulent shear layer

Takumi Akao (赤尾拓海), **Tomoaki Watanabe** (渡邉智昭) **and** **Koji Nagata** (長田孝二)

View Online   Export Citation   CrossMark

Vertical confinement effects on a fully developed turbulent shear layer

View Online　　Export Citation　　CrossMark

Takumi Akao (赤尾拓海),[1] Tomoaki Watanabe (渡邉智昭),[2,a] (iD) and Koji Nagata (長田孝二)[1] (iD)

AFFILIATIONS

[1]Department of Aerospace Engineering, Nagoya University, Furo-cho, Nagoya, Aichi 464-8603, Japan
[2]Education and Research Center for Flight Engineering, Nagoya University, Furo-cho, Chikusa, Nagoya 464-8603, Japan

[a]Author to whom correspondence should be addressed: watanabe.tomoaki@c.nagoya-u.jp

ABSTRACT

The effects of vertical confinement on a turbulent shear layer are investigated with large-eddy simulations of a freely developing shear layer (FSL) and a wall-confined shear layer (WSL) that develops between two horizontal walls. In the case of the WSL, the growth of the shear layer is inhibited by the walls. Once the walls prevent the development of the shear layer, highly anisotropic velocity fluctuations become prominent in the flow. These anisotropic velocity fluctuations are recognized as elongated large-scale structures (ELSS), whose streamwise length is much larger than the length scales in the other directions. Spectral analysis confirms that the turbulent kinetic energy is dominated by the ELSS, whose streamwise length grows continuously. A proper orthogonal decomposition can effectively extract a velocity component associated with the ELSS. The isotropy of the Reynolds stress tensor is changed by the presence of the ELSS. These changes in flow characteristics due to the ELSS are not observed in the FSL, where the shear layer thickness increases continuously. These behaviors of the WSL are consistent with those of stably stratified shear layers (SSSLs), where flow structures similar to ELSS also develop when the vertical flow development is confined by the stable stratification. The vertical confinement by the walls or stable stratification strengthens mean shear effects. The flow behavior at large scales in the WSL and SSSL is consistent with rapid distortion theory for turbulence subject to mean shear, suggesting that the development of ELSS is caused by the mean shear.

Published under an exclusive license by AIP Publishing. https://doi.org/10.1063/5.0090686

I. INTRODUCTION

A turbulent shear layer that develops in two parallel flows with different velocities is one of the most canonical turbulent flows. Many publications have considered the turbulent shear layer as a model system to investigate various phenomena related to turbulence. The formation of large-scale turbulent structures is often studied by flow visualization of developing turbulent shear layers.[1,2] The assumption of self-similarity for turbulent free shear flows has also been tested with experiments and numerical simulations of turbulent shear layers.[3,4] Other studies concern turbulent transport of momentum, energy, and scalars (e.g., temperature and species concentrations), especially because of the practical importance of turbulent mixing in engineering applications.[5–9]

A laminar shear layer develops into a turbulent state by Kelvin–Helmholtz instability. This process for generating turbulence is common in environmental flows. For example, turbulence generated by Kelvin–Helmholtz instability plays an important role in ocean mixing.[10] Large-scale vortices arising from Kelvin–Helmholtz instability are often identified in field observations in the atmosphere.[11,12] These studies have also observed turbulent shear layers with stably

stratified density distributions. Therefore, a number of laboratory experiments and numerical simulations have been carried out for stably stratified shear layers (SSSLs).[13–16] These studies have investigated the effects of stratification on the turbulent transition[17] and on turbulent mixing parameterization (e.g., mixing efficiency).[18,19]

Stratification effects on turbulent structures have also been investigated in SSSLs. Turbulent structures are identified in flow visualization as coherent patterns. Many hairpin vortices are generated in SSSLs,[20,21] although they do not appear in nonstratified turbulent shear layers.[22,23] Furthermore, the large-scale turbulent structures identified in a velocity field are highly anisotropic.[24] These structures have an elongated shape in the streamwise direction and a streamwise length scale much larger than the vertical length scale of the flow. Hairpin vortices and elongated large-scale structures (ELSS) resemble the turbulent structures found in wall turbulence. Hairpin vortices are frequently observed in wall-bounded shear flows.[25] Long turbulent structures whose streamwise length is much larger than the vertical scale, such as a boundary layer thickness, have also been found in the wall-bounded shear flows.[26–30] In addition, the turbulent kinetic energy budget has been analyzed in wavenumber space by employing

the Fourier transform in turbulent channel flows and SSSLs.[24,31] These analyses have revealed that most terms in the energy transport equations have a similar wavenumber dependence in these flows.

The studies described above have confirmed that SSSLs behave similarly to wall-bounded shear flows, although the former develop freely without any influence from the wall. Both flows develop under the influence of the mean shear. Furthermore, it has been pointed out that the wall and stable stratification may play similar roles in suppressing vertical turbulent motions.[21] In wall turbulence, the impermeability condition on the wall inhibits large-scale vertical velocity fluctuations. Similarly, the buoyancy flux in a stably stratified fluid converts the kinetic energy of vertical velocity to potential energy, weakening vertical turbulent motions. Consequently, the vertical length scale of turbulent motions is confined in these flows by the wall or the stable stratification. It is often assumed for wall turbulence that the vertical length scale of the largest turbulent motions at a given point is fixed as a distance from the wall.[32] The vertical length scale of a turbulent shear layer is the shear layer thickness. Stable stratification prevents the growth of shear layer thickness by suppressing vertical momentum transport.[15] ELSS emerge in a SSSL when the effect of stratification is strong enough to prevent shear layer growth in the vertical direction.[24] Thus, the imposition of vertical length scales by stratification can be crucial for the development of ELSS, similar to what occurs in wall turbulence. However, it is not clear if the generation of the ELSS is caused by the vertical confinement due to the stable stratification, because other phenomena in a stratified fluid, such as internal gravity waves, may also affect large-scale turbulent structures.

Previous studies of SSSLs suggest that a turbulent shear layer behaves very differently when its vertical growth is inhibited. This study aims to investigate the effects of vertical confinement on the development of a turbulent shear layer without stable stratification. Here, a freely developing turbulent shear layer is compared with a wall-confined turbulent shear layer that develops between two horizontal walls. These flows are investigated using large-eddy simulations (LES), because our primary interest is the behavior of large-scale turbulent structures. This study considers a temporally developing turbulent shear layer, where the statistics are defined with spatial averages. For this flow, ensemble averages of repeated simulations are necessary to obtain well-converged statistics, especially for quantities related to large-scale turbulent motions. Therefore, LES is more suited for this study than direct numerical simulations (DNS) because of the low computational cost of LES. As shown below, the wall confinement imposes a fixed vertical length scale on the turbulent shear layer, as is also observed in SSSLs. We will show that the effect of wall confinement results in growth of anisotropic velocity fluctuations, which has also been reported in a SSSL.[24] The present results will also be valuable for providing a better understanding of internal turbulent flows with mean shear, such as jets issuing into a confined space[33,34] and shear layers in a narrow channel or duct,[35–37] which are of practical importance in combustors.[38]

The remainder of this paper is organized as follows: Sec. II presents the simulation setup and numerical methods for the freely developing and wall-confined turbulent shear layers. The results are discussed in Sec. III, where the effect of wall confinement is compared with that of buoyancy in SSSLs. Finally, the paper is summarized in Sec. IV.

II. NUMERICAL METHODOLOGY

A. Problem configuration

LES is performed for temporally developing turbulent shear layers. The governing equations are the Navier–Stokes equations for an incompressible fluid. LES solves the governing equations for large-scale (low-pass filtered) components of flow variables, which can be resolved on a computational grid. A variable $f^{(*)}$ is decomposed into grid-scale and subgrid-scale (SGS) components as $f^{(*)} = f + f^{(SGS)}$. The governing equations for the grid-scale velocity are written as

$$\frac{\partial u_j}{\partial x_j} = 0, \tag{1}$$

$$\frac{\partial u_i}{\partial t} + \frac{\partial u_i u_j}{\partial x_j} = -\frac{1}{\rho}\frac{\partial p}{\partial x_i} + \nu\frac{\partial^2 u_i}{\partial x_j \partial x_j} + R_{u_i}, \tag{2}$$

where u_i is the ith component of the velocity vector, x_i is position, t is time, ρ is a constant density, p is pressure, ν is kinematic viscosity, and R_{u_i} is the term arising from the SGS velocity components. Throughout this paper, repeated indices imply summation.

The present study considers two flow setups to investigate the effect of vertical confinement on the turbulent shear layer: one is a conventional, freely developing shear layer (FSL) that is located far from boundaries; the other is a wall-confined shear layer (WSL) that develops between horizontal walls. In the WSL, the vertical growth of the shear layer is prevented by the wall confinement, which is compared with the suppression of the vertical motions in stably stratified turbulence. The former has been extensively studied in the context of turbulent free shear flows.[3,23,39–41]

Figure 1 illustrates the LES of the FSL and WSL. The velocity components in the streamwise (x), vertical (y), and spanwise (z) directions are denoted by u, v, and w, respectively. The computational domain is a rectangular box of dimensions $L_x \times L_y \times L_z$. The temporally developing shear layer is periodic in the x and z directions, for which the flow is statistically homogeneous. An average of a variable $f(x,y,z,t)$ is defined as $\bar{f}(y,t) = (1/L_x L_z)\iint f\,dx\,dz$, where the integral is taken in a horizontal plane. Fluctuations of f are denoted by $f'(x,y,z,t) = f(x,y,z,t) - \bar{f}(y,t)$ and the root mean square (rms) of the fluctuations is calculated as $f_{rms}(y,t) = (\overline{f'^2})^{1/2} = (\overline{f^2} - \bar{f}^2)^{1/2}$. Following previous studies of temporally developing shear layers,[23] the initial mean streamwise velocity profile is given by $\bar{u} = 0.5U_0\tanh(2y/h_0)$, where U_0 is the difference in streamwise velocity between the upper and lower regions and h_0 is the initial shear layer thickness. The nondimensional parameter of the flow is the Reynolds number, defined as $Re = U_0 h_0/\nu$. The FSL and WSL are simulated for $Re = 2000$. The mean velocities in other directions are zero. Artificial velocity fluctuations with rms values of $0.025U_0$ are superimposed on the initial mean velocity in the shear layer ($|y| \leq h_0/2$) for triggering the turbulent transition. Here, the fluctuations are generated with the method for converting random numbers to spatially correlated fluctuations described in Refs. 24 and 42. Time is advanced until $t/t_r = 340$, where $t_r = h_0/U_0$ is a reference timescale of the shear layer.

The main differences between the FSL and WSL are the boundary conditions and the size of the computational domain in the vertical direction. Periodic boundary conditions are applied in the streamwise (x) and spanwise (z) directions in both flows. The vertical (y)
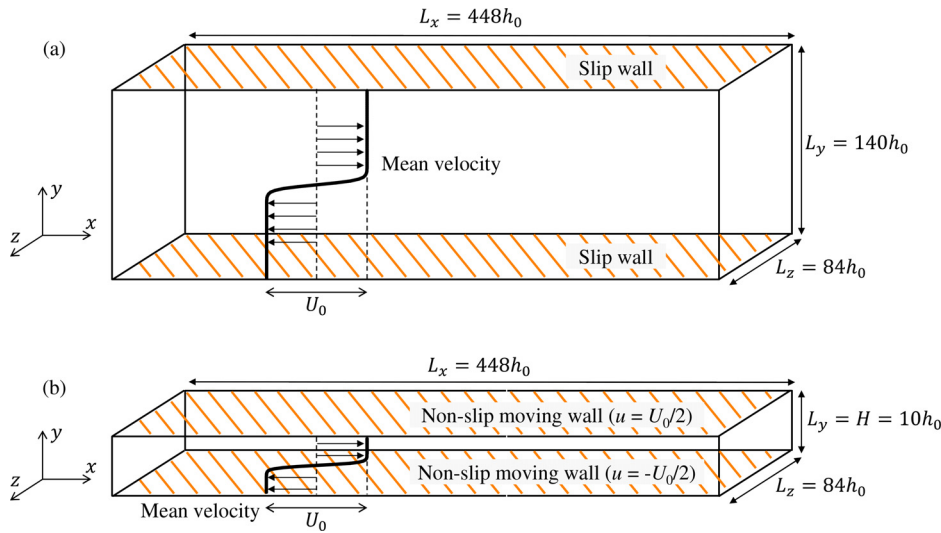
FIG. 1. LES of (a) a freely developing shear layer (FSL) and (b) a wall-confined shear layer (WSL).

boundaries are treated as slip walls for the FSL and nonslip walls moving with a streamwise velocity of $\pm U_0/2$ for the WSL (Fig. 1). The moving walls are considered in the WSL to maintain the mean shear, since the present study aims to investigate the development of the shear layer under wall confinement. The size of the computational domain (L_x, L_y, L_z) is $(448h_0, 140h_0, 84h_0)$ for the FSL and $(448h_0, 10h_0, 84h_0)$ for the WSL. In the FSL, the shear layer thickness grows up to $30h_0$ at the end of the simulation, and $L_y = 140h_0$ is large enough to prevent the boundaries from affecting the shear layer development. The distance between the walls is also denoted by $H = 10h_0$ in the WSL. The shear layer development of the WSL is influenced by the walls as the shear layer thickness approaches H. The domain height $10h_0$ is chosen to compare the WSL with a SSSL in Ref. 24, for which the thickness of the shear layer is about $10h_0$. Because wall influences are examined for a fully developed turbulent shear layer, L_y should be large enough for the initial shear instability to be free from the wall influences. As shown by comparison between the FSL and WSL below, the initial development of the shear layers hardly differs for these flows when the WSL is simulated with $L_y = 10h_0$. In the LES of the WSL, a turbulent Couette flow develops if the simulation is run for a long time. The instantaneous flow fields before the Couette flow has fully developed are analyzed to investigate the effect of wall confinement on the shear layer.

B. Numerical setup

The LES is performed with an in-house implicit LES code, which was also used in our previous studies of turbulent free shear flows and wall turbulence.[24,42,43] These previous studies validated the code by comparing the LES results with experiments and direct numerical simulations (DNS). The code is based on a fractional step method with finite difference schemes. Fully conservative finite difference schemes are used for spatial derivatives, with fourth- and second-order accuracies in the horizontal and vertical directions, respectively.[44] Variables are stored on a staggered grid. The grid size is uniform in the horizontal directions, while nonuniform grid spacing is employed in the vertical direction, as explained below. A third-order Runge–Kutta method is used for temporal advancement. The biconjugate gradient stabilized (Bi-CGSTAB) method is used to solve the Poisson equation for pressure. The present implicit LES utilizes the 10th-order low-pass filter proposed in Ref. 45 as an implicit model of the SGS terms. A variable f at a grid point (i, j, k) is denoted by $f_{i,j,k}$. The filtering operator in the x direction, F_x, is written as

$$F_x * f = f_{i,j,k} - 2^{-10} \big[252 f_{i,j,k} - 210(f_{i+1,j,k} + f_{i-1,j,k})$$
$$+ 120(f_{i+2,j,k} + f_{i-2,j,k}) - 45(f_{i+3,j,k} + f_{i-3,j,k})$$
$$+ 10(f_{i+4,j,k} + f_{i-4,j,k}) - (f_{i+5,j,k} + f_{i-5,j,k})\big]. \quad (3)$$

The filters in the y and z directions, F_y and F_z, are also written in the same manner. The filters are sequentially applied in three directions as $F(f) \equiv F_x * [F_y * (F_z * f)]$. Then, the SGS term R_{u_i} in Eq. (2) is written with the filter $F(f)$ as

$$R_{u_i} = \frac{F(u_i) - u_i}{\Delta t}, \quad (4)$$

where Δt is a time increment. The low-pass filter in implicit LES mimics the energy dissipation that takes place on unresolved scales. Equation (4) is equivalent to applying the filter to u_i at every time step. The simulations of both the FSL and WSL are repeated 10 times, and ensemble averages are taken for 10 simulations. Each simulation uses different sets of random numbers, which are generated with different seeds. The statistical properties of initial velocity fluctuations are identical for all simulations. The energy spectrum of initial velocity fluctuations generated by the present method has been presented in Refs. 24 and 42.

The numbers of grid points are $(N_x, N_y, N_z) = (3072, 251, 576)$ in the WSL and $(3072, 701, 576)$ in the FSL. The vertical location of the grid points is determined by

$$y(j) = -\frac{L_y}{2\alpha_y} \text{artanh}\left[(\tanh \alpha_y)\left(1 - 2\frac{j-1}{N_y - 1}\right)\right] \quad (5)$$
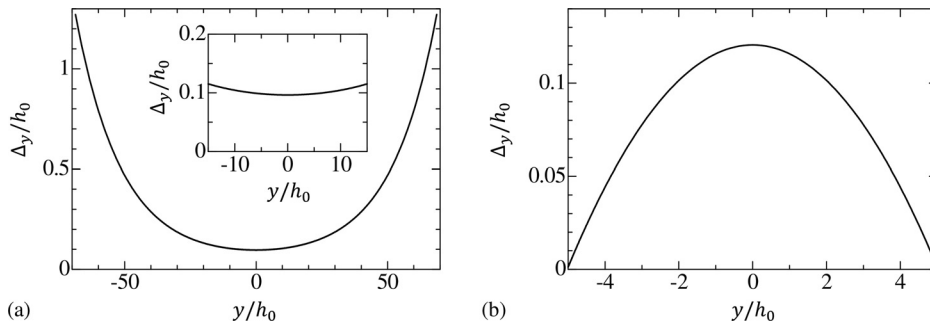
FIG. 2. Vertical distribution of grid spacing in the y direction in the LES of (a) the FSL and (b) the WSL.

for the FSL and

$$y(j) = -\frac{L_y}{2\tanh\alpha_y}\tanh\left[\alpha_y\left(1 - 2\frac{j-1}{N_y - 1}\right)\right] \quad (6)$$

for the WSL, with integers $j = 1, \ldots, N_y$. The grid stretching parameter is $\alpha_y = 2$ for the FSL and $\alpha_y = 3$ for the WSL. Figure 2 shows the vertical distribution of the grid size in the y direction, $\Delta_y(y)$. The turbulent shear layer does not reach large $|y|$ in the FSL. For this reason, the LES of the FSL employs Eq. (5), which yields the smallest $\Delta_y(y)$ at $y = 0$. The turbulent shear layer develops in the y direction with time and reaches $|y/h_0| \approx 15$ at the end of the simulation of the FSL. The inset in Fig. 2(a) shows $\Delta_y(y)$ for $|y/h_0| \lesssim 15$, where $\Delta_y(y) \approx 0.1$ hardly varies with y. On the other hand, a high resolution is also required near the boundaries for the WSL because of the development of wall turbulence. Therefore, the LES of WSL employs Eq. (6), for which $\Delta_y(y)$ becomes small near the walls. Here, $\Delta_y(y)$ near the walls is small enough to resolve the viscous sublayers on the walls. This will be confirmed in Sec. III, where the mean velocity profile near the wall is presented. Inside the shear layers, the spatial resolution should be

determined based on the Kolmogorov scale $\eta = (\nu^3/\varepsilon)^{1/4}$, where ε is the turbulent kinetic energy dissipation rate. DNS of the FSL with the same Re as in the present LES was reported in Refs. 21 and 24, where the smallest value of η is about $0.02h_0$ at $t/t_r = 90$. The FSL and WSL develop similarly before the entire computational domain between the walls is occupied by turbulence in the WSL. The turbulent shear layer in the WSL has not reached the walls at $t/t_r = 90$, and the smallest η in the WSL is also close to $0.02h_0$. In this study, the FSL and WSL are simulated with $(\Delta_x, \Delta_y, \Delta_z)$ $= (0.15h_0, 0.096h_0, 0.15h_0)$ and $(0.15h_0, 0.12h_0, 0.15h_0)$, respectively, where Δ_y is evaluated at $y = 0$. Thus, the grid spacing is smaller than 10η, and most length scales are well resolved in the LES. The present LES code with $\Delta_i \approx 10\eta$ can accurately simulate turbulent shear flows and wall turbulence.[24,42]

III. RESULTS AND DISCUSSION

A. Development of turbulent shear layers

Figure 3 visualizes the development of the FSL with the instantaneous streamwise velocity profiles on an x–y plane at $t/t_r = 60$,
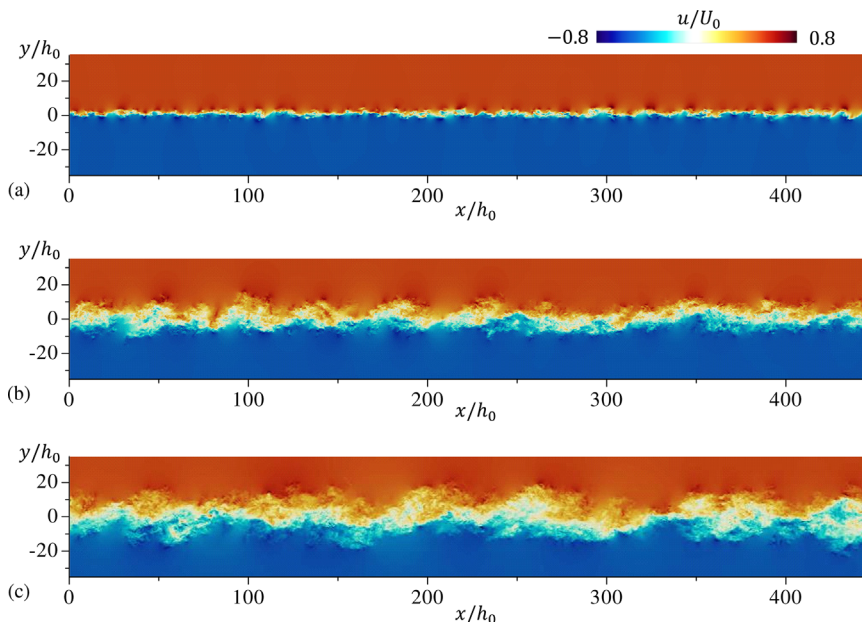

FIG. 3. Instantaneous streamwise velocity on an x–y plane in the FSL at (a) $t/t_r = 60$, (b) $t/t_r = 180$, and (c) $t/t_r = 300$. The visualized region in the vertical direction is a half of the domain height L_y.

180, and 300. The range of the color contours is determined based on the maximum and minimum values of u/U_0. Although u/U_0 at $t = 0$ ranges between -0.5 and 0.5, an instantaneous velocity can exceed this range because large-scale vortices locally accelerate or deaccelerate the flow. This influence can be explained by a pressure gradient induced by the vortices.[46] A similar fluid acceleration by vortices arising from shear instability has also been reported for a turbulent jet, where an instantaneous velocity exceeds the jet velocity at a nozzle exit.[47,48] The shear layer has already become turbulent at $t/t_r = 60$ as a result of Kelvin–Helmholtz instability. The turbulent shear layer develops with time in the y direction. The results for the WSL are shown in Fig. 4, where u is shown either in the entire computational domain or in a small domain with a streamwise length of $114h_0$ (a rectangular box outlined with dashed lines). At $t/t_r = 60$, the velocity fluctuations in the turbulent shear layer are found near the center of the layer, although the turbulent region of the layer does not reach the walls. At $t/t_r = 180$ and 300, the turbulent shear layer has developed in the entire computational domain, and the flow evolution is expected to be strongly influenced by the walls.

Figure 5(a) shows the vertical profiles of the mean streamwise velocity $\bar{u}$ in the FSL. Here, y is normalized by the momentum thickness $\delta_m = \frac{1}{4} \int (U_0 - 2\bar{u})(U_0 + 2\bar{u}) \, dy$. The mean velocity profile plotted with y/δ_m hardly varies with time as expected for a self-similar regime. Figure 5(b) compares the rms fluctuations of u, u_{rms}, with previous experiments and numerical simulations of turbulent shear layers.[49,50] From $t/t_r = 60$ to 140, u_{rms} decreases slightly with time. In a self-similar turbulent shear layer, u_{rms} at $y = 0$ does not change with the development of the shear layer.[51] This tendency is also seen after $t/t_r = 140$ in the present LES. Furthermore, the LES results agree well

with previous studies, and the development of the turbulent shear layer is accurately predicted by the LES.

Figure 6(a) shows the mean velocity profile $\bar{u}$ in the WSL. At $t/t_r = 60$, $\bar{u}$ has a similar profile in the FSL and WSL, and the mean velocity gradient $\partial\bar{u}/\partial y$ is close to 0 for large $|y|$. At this time, the turbulent shear layer has not yet reached the walls. However, $\partial\bar{u}/\partial y$ at $y/H = \pm 0.5$ becomes large at later times in the WSL once the turbulent shear layer has developed in the entire computational domain. Figures 6(b)–6(d) show the vertical profiles of u_{rms}, v_{rms}, and w_{rms}. The velocity fluctuations become small near the walls, and the rms velocity fluctuations decrease to zero toward $y/H = \pm 0.5$. The shape of the rms velocity profiles changes with time. As the turbulent shear layer develops toward the walls from $t/t_r = 60$, the rms velocity fluctuations near the walls increase with time. At $t/t_r = 300$, u_{rms} has peaks near the walls at $y/H \approx \pm 0.49$. Compared with u_{rms} and w_{rms}, v_{rms} is small near the walls ($|y/H| \gtrsim 0.3$), because of the suppression of vertical velocity fluctuations.

In the case of the WSL, the flow approaches a fully developed Couette flow with time. The present study considers the influence of the walls on the development of the shear layer, which is not directly related to the Couette flow generated by the walls. Therefore, the WSL and FSL should be compared for the time before wall turbulence has fully developed in the WSL. This time interval can be determined by comparing the velocity statistics near the walls in the WSL with those in canonical wall-bounded turbulent flows. Figure 7 shows a comparison of mean and rms fluctuations of streamwise velocity between the WSL and wall turbulence. Here, the results for the WSL are plotted against the distance from the bottom wall, $y_w = y + H/2$. The variables are normalized by viscous units as $y^+ = (y + H/2)/(\nu/u_\tau)$, $u^+ = \bar{u}/u_\tau$, and
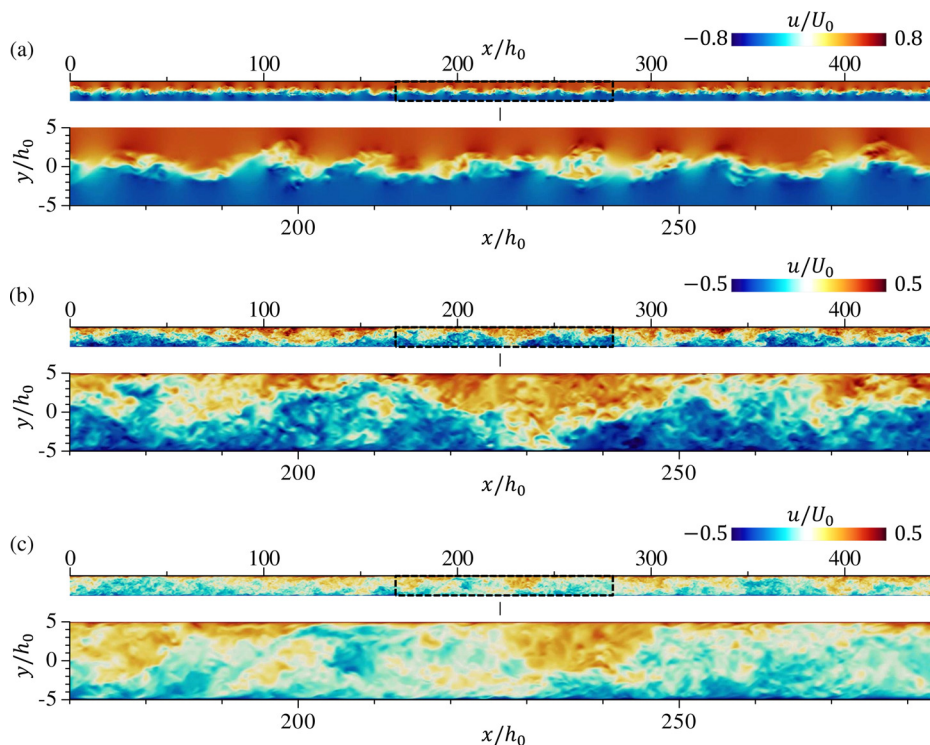

FIG. 4. Instantaneous streamwise velocity on an x–y plane in the WSL at (a) $t/t_r = 60$, (b) $t/t_r = 180$, and (c) $t/t_r = 300$. In each panel, the upper FIG shows the entire computational domain, while the black dashed rectangle outlines a partial domain that is visualized in the lower FIG.
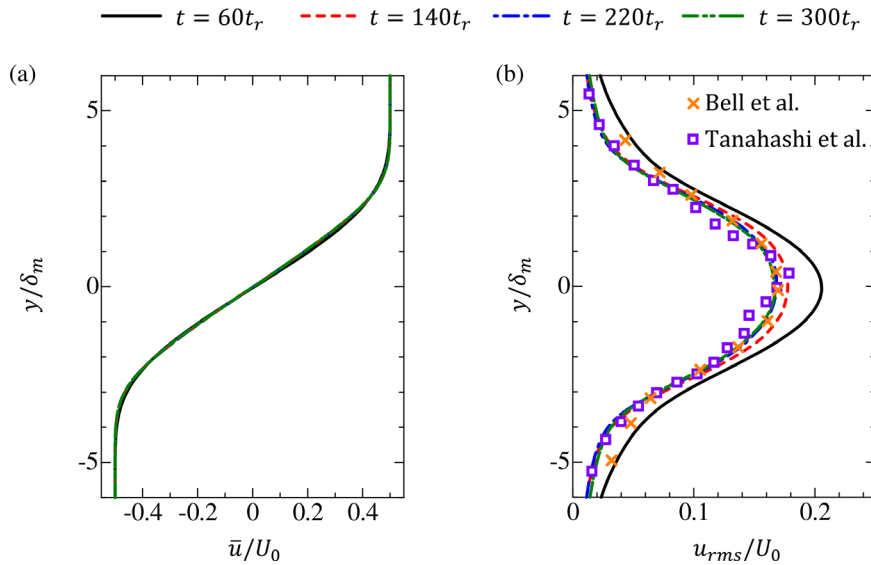
FIG. 5. Vertical profiles of (a) mean streamwise velocity $\bar{u}$ and (b) rms fluctuations of u, u_{rms}, in the FSL. The vertical position y is normalized by the momentum thickness δ_m. The results of experiment[49] and DNS[50] are shown for comparison.

$u_{rms}^+ = u_{rms}/u_\tau$, where $u_\tau = \sqrt{\tau_W/\rho}$ is the friction velocity defined with the wall shear stress $\tau_W = \rho\nu\partial\bar{u}/\partial y$. In Fig. 7(a), the mean velocity profiles are compared with the profiles in the viscous sublayer $u^+ = y^+$ and the logarithmic layer $u^+ = (1/\kappa)\ln(y^+) + A$ with $\kappa = 0.41$ and $A = 5.1$. For $y^+ \lesssim 6$, the mean velocity profile in the WSL follows $u^+ = y^+$. The logarithmic law is expected to be observed for $y^+ \gtrsim 30$ in fully developed wall turbulence.[51] However, the WSL has u^+ smaller than the logarithmic law, although the mean velocity profile becomes closer to the logarithmic law with time. Therefore, the logarithmic layer has not yet fully formed in the WSL, even at $t/t_r = 340$. Figure 7(b) compares the vertical profile of u_{rms}^+ between the WSL and turbulent Couette flows.[52,53] The profile of u_{rms}^+ approaches those in fully developed turbulent Couette flows with time. However, the difference between the WSL and the turbulent Couette flows is still large at $t/t_r = 340$, and the WSL has not yet developed into turbulent Couette flow. The temporal variations of u^+ and u_{rms}^+ suggest that the wall turbulence is still under development even at $t/t_r = 340$. Therefore, the present LES results for $t/t_r \leq 340$ are suitable for the investigation of the influence of the walls on the turbulent shear layer.

The dissipation of turbulent kinetic energy is caused by the grid-scale velocity fluctuations and the SGS model in the LES. The dissipation rate ε can be expressed as the sum of the contributions from the grid scales and the model as $\varepsilon = \varepsilon_G + \varepsilon_S$, where ε_G and ε_S for the implicit SGS model can be written as

$$\varepsilon_G = \nu\overline{\frac{\partial u_i'}{\partial x_j}\frac{\partial u_i'}{\partial x_j}}, \quad \varepsilon_S = -\overline{u_i'F(u_i')}. \tag{7}$$

The implicit LES can accurately evaluate the energy dissipation rate with Eq. (7).[24,48] Figure 8 shows the temporal evolution of ε at the center of the WSL and FSL. Once the turbulent shear layer develops, ε decays with time. The decay is faster in the WSL than in the FSL. The self-similar assumption for a temporally developing shear layer yields a power law of $\varepsilon \sim t^{-1}$. This power law is observed after $t/t_r \approx 180$ in the FSL.

Figure 8(b) shows the evolution of the turbulent Reynolds number on the centerline, $Re_\lambda = u_0\lambda/\nu$, which is defined with the rms velocity fluctuation $u_0 = \sqrt{(\langle u'^2\rangle + \langle v'^2\rangle + \langle w'^2\rangle)/3}$ and the Taylor microscale $\lambda = \sqrt{15\nu u_0^2/\varepsilon}$. The turbulence generated by the instability has $Re_\lambda \approx 200$ at $t/t_r = 60$. Then, Re_λ in the FSL becomes large with time because of an increase in λ. However, Re_λ in the WSL decreases because of the decay of u_0, which is shown in Fig. 6.

B. Length scales of large-scale velocity fluctuations

The characteristic length scales of the flow are compared between the FSL and WSL. One of the vertical length scales is the shear layer thickness δ_u, which is defined with the mean velocity profile as the distance between two vertical positions with $\bar{u}/U_0 = \pm 0.45$. Figure 9 shows the temporal evolution of δ_u normalized by h_0. Figure 9 also includes data for a SSSL,[24] which is discussed in Sec. III D. As also reported in previous studies of freely developing turbulent shear layers, δ_u in the FSL increases continuously with time. The rate of increase in δ_u becomes slightly lower at a late time, which is in a self-similar regime of the turbulent shear layer. This tendency is also consistent with previous studies.[46,54] The initial increase in δ_u is similar in the FSL and WSL until $t/t_r \approx 100$. The thickness of the WSL is restricted to $\delta_u/h_0 \leq 10$ by the walls, and $\delta_u \approx 10h_0$ is constant after $t/t_r = 100$. The constant value of δ_u suggests that the vertical turbulent motions are strongly influenced by the walls for $t/t_r \gtrsim 100$.

Figures 10 and 11 visualize the instantaneous streamwise velocity u on the x–z plane at $y = 0$, which is the center of the shear layer. The arrows near the top left of each panel depict the length of δ_u, which is visibly compared with horizontal length scales of the flows. The length scale of u becomes large with time in both the FSL and WSL. In the FSL, δ_u also increases with time. Therefore, the length scale of u, roughly estimated as the size of each region with $u > 0$ or $u < 0$, is close to δ_u in Fig. 10. The results for the WSL suggest that the streamwise length scale of u also increases from $t/t_r = 60$ to 300, while the vertical length δ_u does not grow after $t/t_r \approx 100$. Therefore, the length-scale ratio of u between the streamwise and vertical directions
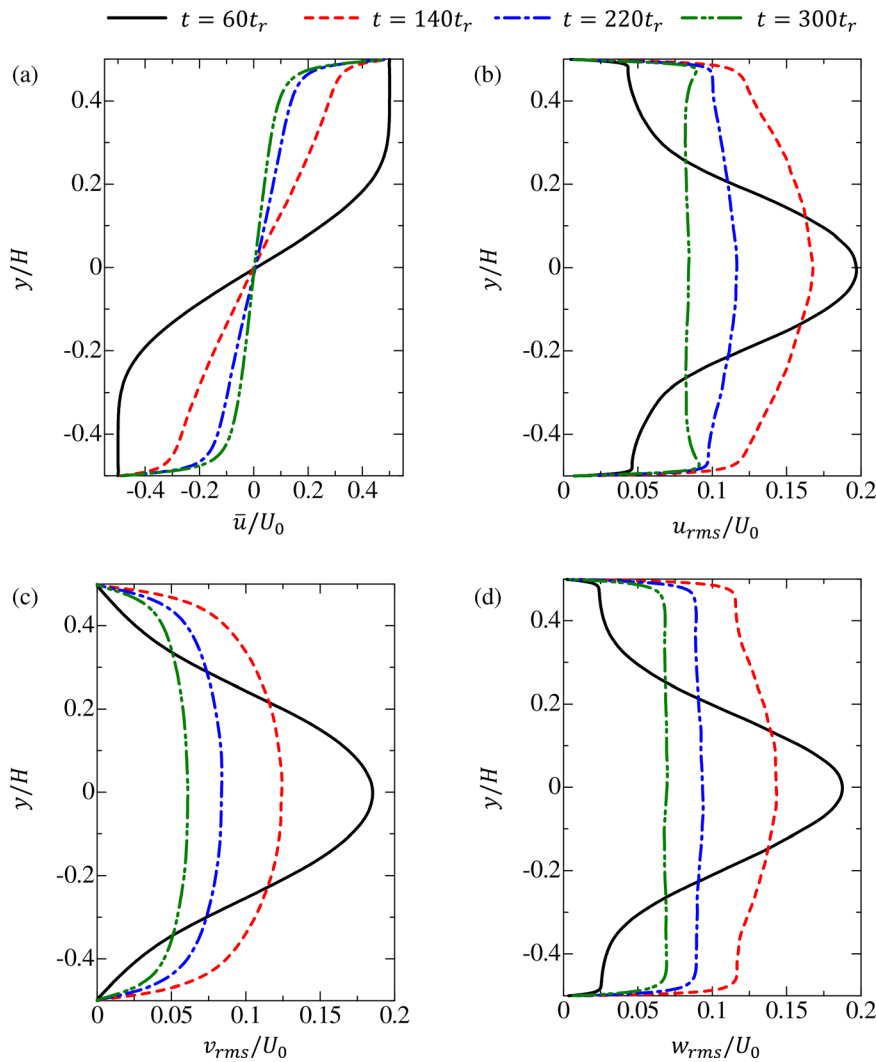
FIG. 6. (a) Vertical profile of mean streamwise velocity $\bar{u}$. (b), (c), and (d) Vertical profiles of rms fluctuations of streamwise, vertical, and spanwise velocity components, respectively, in the WSL. The vertical position y is normalized by the distance H between the walls.
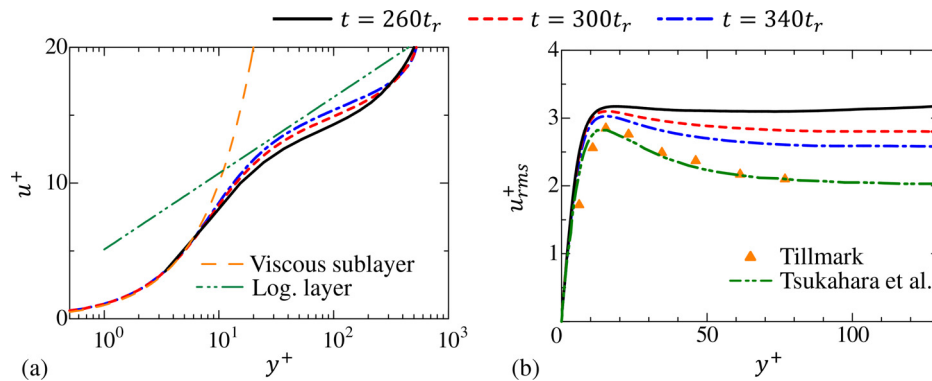

FIG. 7. Vertical profiles of (a) mean streamwise velocity $u^+ = \bar{u}/u_\tau$ and (b) rms fluctuations of streamwise velocity $u^+_{\rm rms} = u_{\rm rms}/u_\tau$ normalized by the friction velocity u_τ near the bottom wall of the computational domain. The vertical distance from the wall, $y_w = y + H/2$, is normalized by ν/u_τ as $y^+ = (y + H/2)/(\nu/u_\tau)$. The mean velocity profile in (a) is compared with the profiles in the viscous sublayer ($u^+ = y^+$) and the logarithmic layer [$u^+ = (1/\kappa)\ln y^+ + A$ with $\kappa = 0.41$ and $A = 5.1$] of wall turbulence. In (b), the present results are compared with experiments and DNS of turbulent Couette flows by Tillmark[52] and Tsukahara et al.[53]
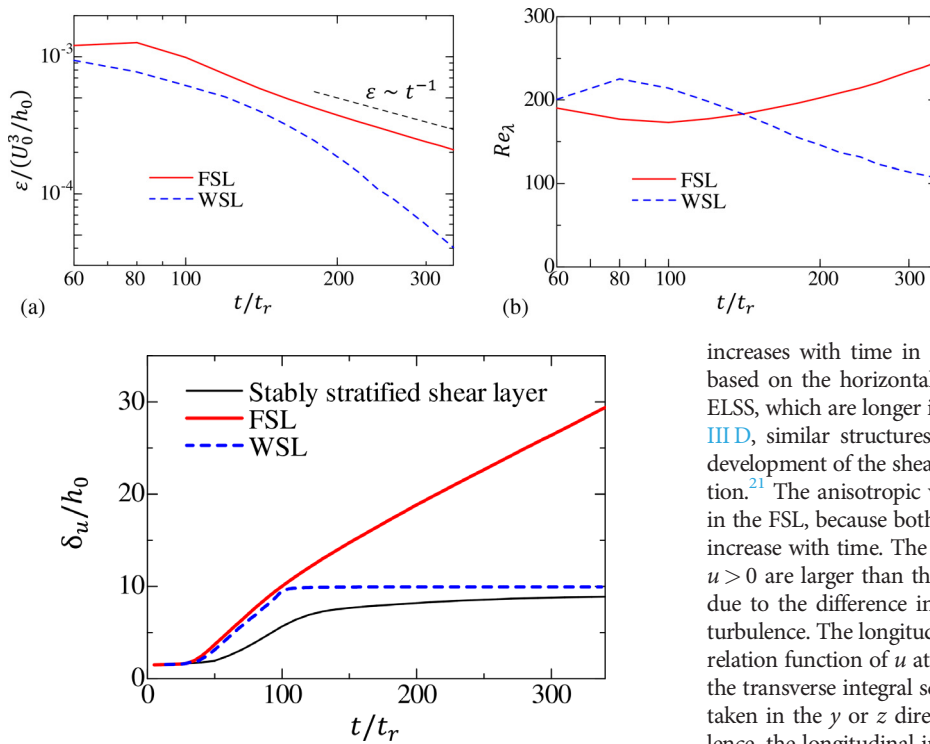
FIG. 9. Temporal evolution of the shear layer thickness δ_u. The LES result for a SSSL[24] is shown for comparison.

increases with time in the WSL. If turbulent structures are defined based on the horizontal profiles of u in Fig. 11(c), one can identify ELSS, which are longer in the x direction than δ_u. As discussed in Sec. III D, similar structures were observed in SSSLs, where the vertical development of the shear layer is also inhibited by the stable stratification.[21] The anisotropic velocity fluctuations of the ELSS do not grow in the FSL, because both the horizontal and vertical length scales of u increase with time. The streamwise lengths of regions with $u < 0$ and $u > 0$ are larger than their spanwise lengths, even in the FSL. This is due to the difference in longitudinal and transverse length scales of turbulence. The longitudinal integral scale is defined with the autocorrelation function of u at two points separated in the x direction, while the transverse integral scale of u is defined for the separation distance taken in the y or z direction. Even in homogeneous isotropic turbulence, the longitudinal integral scale is twice as large as the transverse scale.[32] This explains why the streamwise length scale of u is larger than the spanwise one when these scales are estimated from Fig. 10.
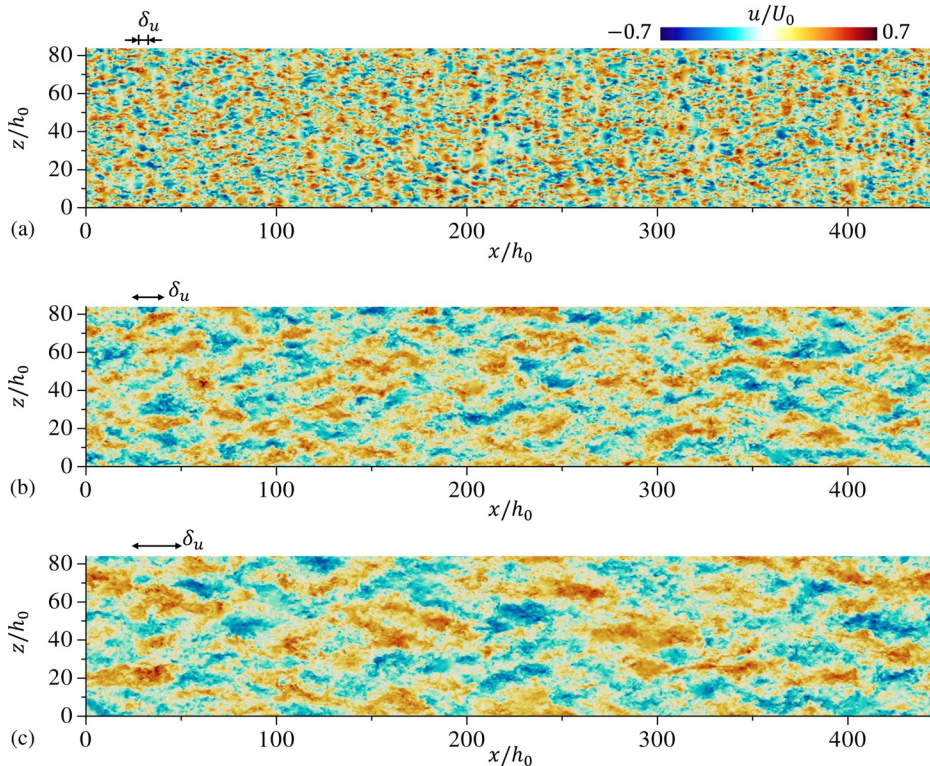

FIG. 10. Instantaneous streamwise velocity profiles on the x–z plane at the center of the shear layer ($y = 0$) in the FSL at (a) $t/t_r = 60$, (b) $t/t_r = 180$, and (c) $t/t_r = 300$.
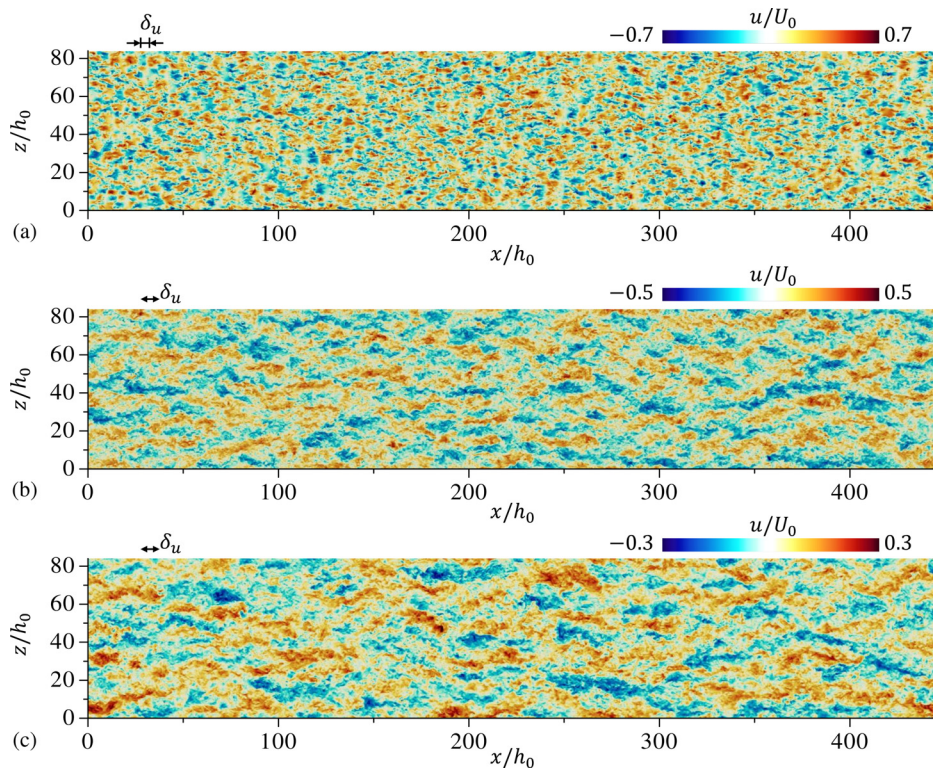
FIG. 11. The same as in Fig. 10, but for the WSL. (a) $t/t_r = 60$, (b) $t/t_r = 180$, and (c) $t/t_r = 300$.

The scale dependence of velocity fluctuations is investigated with a one-dimensional energy spectrum of u. Here, the energy spectrum E_u is calculated using the Fourier transform in the x or z direction. The Fourier transform of $u(x, y, z, t)$ in the x direction is denoted by $\hat{u}(k_x, y, z, t)$, where k_x is the streamwise wavenumber. The fast Fourier transform is employed for converting u to $\hat{u}$. The energy spectrum of u is defined with the complex conjugate of $\hat{u}$, $\hat{u}^*(k_x, y, z, t)$, as $E_u(k_x, y, t) = \text{Re}(\widehat{\hat{u}\hat{u}^*})$, where $\text{Re}(f)$ represents a real part of a complex variable f. The average $\widehat{\hat{u}\hat{u}^*}$ is evaluated with the spatial average in the z direction and the ensemble average of simulations. The energy spectrum for the spanwise wavenumber k_z is similarly defined with the Fourier transform of u in the z direction, $\hat{u}(x, y, k_z, t)$, for which the spatial average of $\hat{u}\hat{u}^*$ is taken in the x direction. The energy spectra are presented as function of the streamwise and spanwise wavelength, $\lambda_x = 2\pi/k_x$ and $\lambda_z = 2\pi/k_z$.

Figure 12 shows $k_x E_u$ as a function of (λ_x, y) at $t/t_r = 60$, 180, and 300, where panels (a)–(c) and (d)–(f) present the results for the FSL and WSL, respectively. Because of the symmetry of the flow with respect to $y = 0$, the results are shown for $y \geq 0$. The horizontal axis displays $\lambda_x = 2\pi/k_x$ on a logarithmic scale. Therefore, the spectrum premultiplied by k_x, $k_x E_u$, is shown instead of E_u to assess the contribution to the velocity variance at each height. Because of the relations $k_x d(\log_{10} k_x) = dk_x$ and $\log_{10} k_x \propto -\log_{10} \lambda_x$, $k_x E_u$ represents the contribution to u_{rms}^2 at the scale of λ_x on the logarithmic coordinate. For this reason, the spectra premultiplied by k_x have been widely used to investigate the scale dependence of velocity fluctuations in turbulence.[26,46,55,56] Both horizontal and vertical axes of Fig. 12 are nondimensionalized by δ_u. At each y position, $k_x E_u$ in the FSL

[Figs. 12(a)–12(c)] has a peak at $\lambda_x/\delta_u \approx 3$, and the spectral shape hardly varies with time. Furthermore, $k_x E_u$ decreases with y, because the outside of the turbulent shear layer has smaller velocity fluctuations than the inside. By contrast, $k_x E_u$ in the WSL depends strongly on time in Figs. 12(d)–12(f). A wavelength range with large $k_x E_u$ extends to larger scales with time in the WSL, and the velocity fluctuations are dominated by streamwise length scales much larger than δ_u. This change in the dominant length scale is associated with the formation of ELSS visualized in Fig. 11. Furthermore, the y dependence of $k_x E_u$ is similar between the FSL and WSL at $t/t_r = 60$, which is before the turbulent shear layer reaches the walls in the WSL. However, the wavenumber dependence of $k_x E_u$ at $t/t_r = 180$ and 300 is different in these flows at $y/\delta_u \approx 0.5$. At this height, $k_x E_u$ in the FSL becomes small as λ_x decreases from $\lambda_x/\delta_u \approx 3$, while $k_x E_u$ in the WSL is moderately large for $0.2 \lesssim \lambda_x/\delta_u \lesssim 2$. Thus, small-scale turbulent motions are negligible at large y in the FSL, while they are active in the WSL even at $y/\delta_u \approx 0.5$. This difference is explained by the outer intermittency of the FSL: the turbulent fluid coexists with the nonturbulent fluid at large y, where small-scale fluctuations are absent in the nonturbulent region.[39,41] On the other hand, the entire flow region between the walls is occupied by turbulence arising from the shear instability after $t/t_r \approx 100$ in the WSL. Therefore, the energy of velocity fluctuations is also possessed by small scales of $0.2 \lesssim \lambda_x/\delta_u \lesssim 2$ in the WSL.

Figures 13(a) and 13(b) show $k_x E_u/(k_x E_u)_{\text{max}}$ at $y = 0$ in the FSL and WSL for detailed comparisons between these flows. At $t/t_r = 60$, the shape of $k_x E_u$, including the peak wavelength $\lambda_x/\delta_u \approx 3$, is similar for the FSL and WSL because the WSL has not yet reached the walls. The normalized peak wavelength in the FSL hardly varies with time
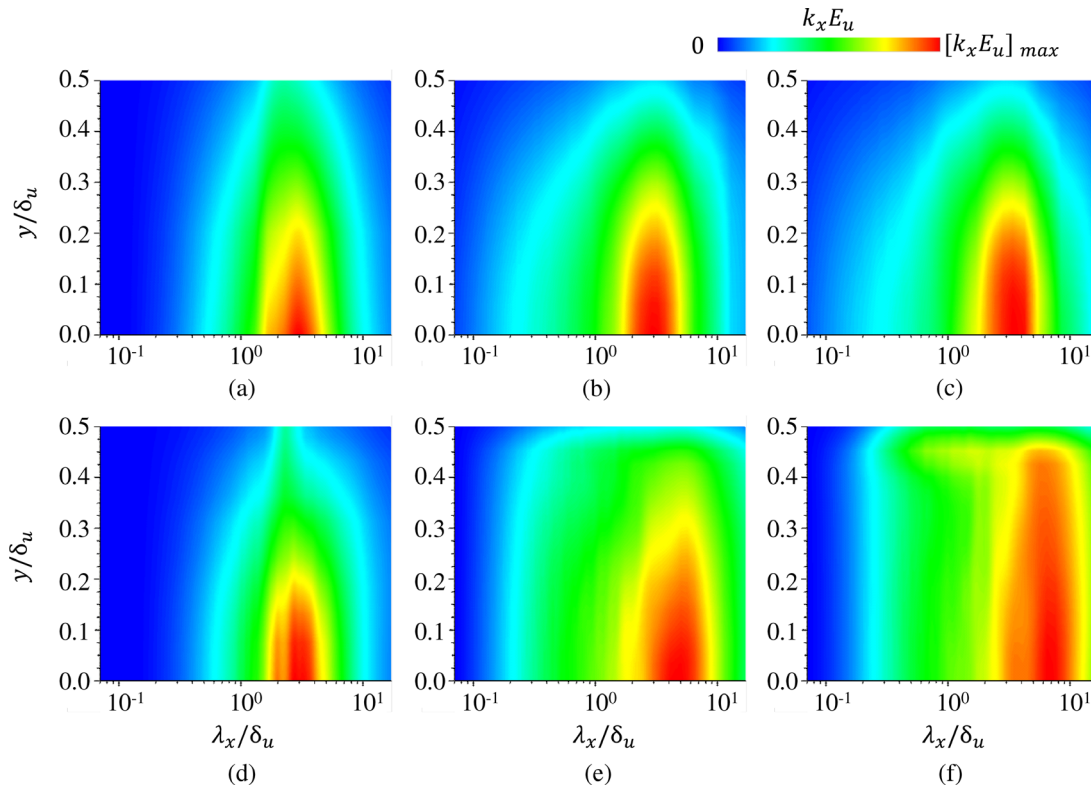
FIG. 12. Premultiplied energy spectra of streamwise velocity, $k_x E_u(k_x)$, plotted as a function of streamwise wavelength λ_x and vertical location y in (a)–(c) the FSL and (d)–(f) the WSL: (a) and (d) $t/t_r = 60$; (b) and (e) $t/t_r = 180$; (c) and (f) $t/t_r = 300$. The color contours are adjusted with the maximum value of $k_x E_u$ at each time to compare the energy distribution at different times.

from $\lambda_x/\delta_u \approx 3$, although the peak wavelength is shifted to larger scales in the WSL. Figure 14 shows the spanwise energy spectrum calculated with the Fourier transform in the z direction. The spanwise spectrum $E_u(k_z)$ is premultiplied by k_z and is plotted against λ_z. The peak of $k_z E_u(k_z)$ appears for $1 \lesssim \lambda_z/\delta_u \lesssim 2$ in both flows. Compared with the energy spectrum plotted with λ_x, the wavelength of the maximum $k_z E_u(k_z)$ slowly increases with time in the WSL.

The temporal variation of the length scales is investigated with the peak wavelengths of $k_x E_u(k_x)$ and $k_z E_u(k_z)$, which are denoted by Λ_x and Λ_z, respectively. The peak wavelength represents the

energy-containing length scale in each direction. Figure 15 shows the temporal variations of Λ_x and Λ_z, which are calculated from the spectra between $t/t_r = 60$ and 340. Figure 15(a) also shows LES results for a SSSL,[24] which are compared with the FSL and WSL in Sec. III D. In Fig. 15(a), both the FSL and WSL have $\Lambda_x/\delta_u \approx 3$ until $t/t_r = 100$. However, Λ_x/δ_u in the WSL begins to increase from $t/t_r = 120$, while $\Lambda_x/\delta_u \approx 3$ does not vary with time in the FSL. The increase in Λ_x/δ_u in the WSL is approximated well by a power law in t, and a least squares method yields $\Lambda_x/\delta_u = 0.117(t/t_r)^{0.72}$. Similarly, Λ_z/δ_u slowly increases with time in the WSL, while $\Lambda_z/\delta_u \approx 1$ does not
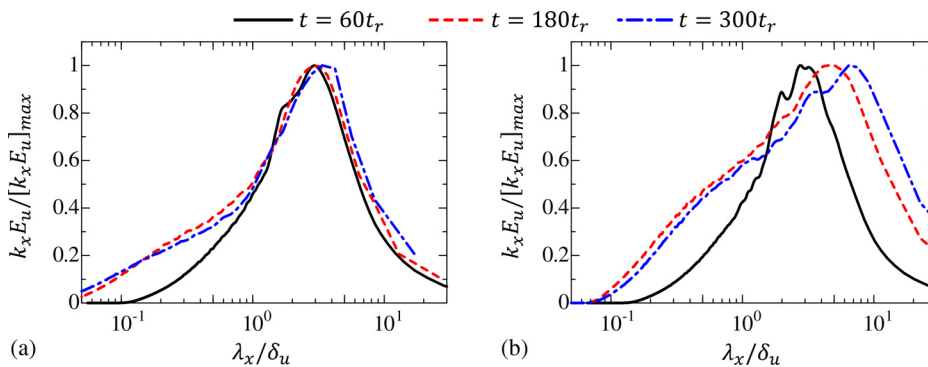

FIG. 13. Premultiplied streamwise-wavenumber spectra of streamwise velocity, $k_x E_u(k_x)$, at the center of the shear layer ($y = 0$) at $t/t_r = 60$, 180, and 300 in (a) the FSL and (b) the WSL. Here, $k_x E_u$ is normalized by its maximum value $[k_x E_u]_{max}$ at each time.
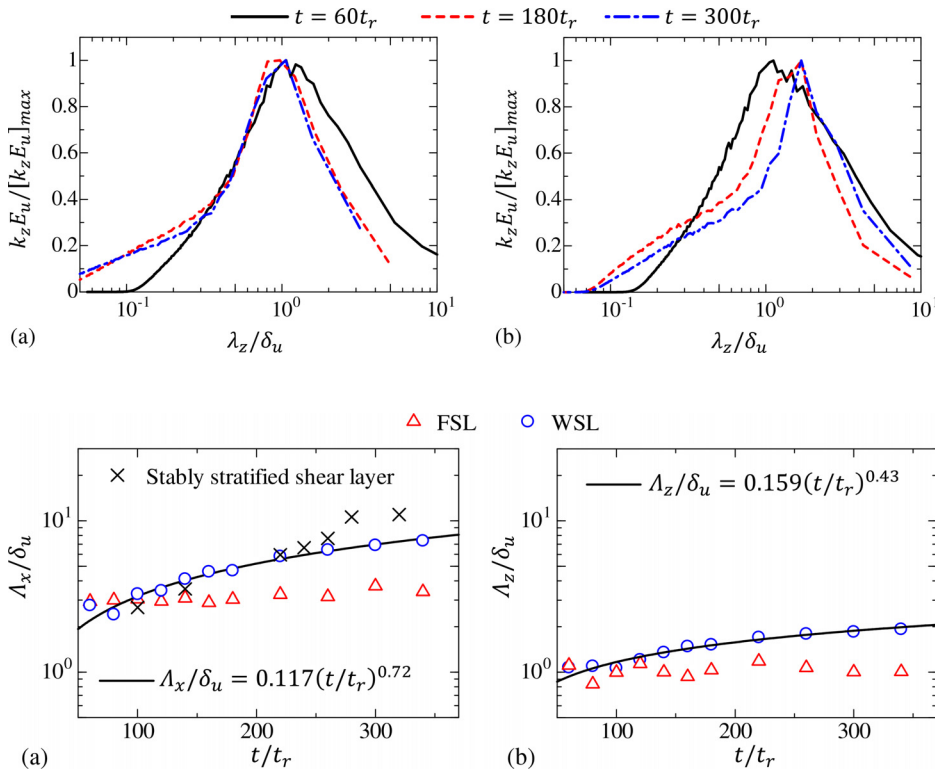
FIG. 14. Premultiplied spanwise-wavenumber spectra $k_z E_u(k_z)$ in (a) the FSL and (b) the WSL. The same normalization as in Fig. 13 is adapted in this FIG.

FIG. 15. Temporal variations of (a) Λ_x and (b) Λ_z at $y = 0$ in the FSL and WSL, where Λ_x and Λ_z are the peak wavelengths of $k_x E_u(k_x)$ and $k_z E_u(k_z)$, respectively. The black solid lines indicate power laws that approximate the data for $t/t_r \geq 120$ in the WSL. The LES results for a SSSL[24] are shown in (a) for comparison.

increase in the FSL. From Fig. 15(b), $\Lambda_z/\delta_u \sim (t/t_r)^{0.43}$ is obtained for the WSL after $t/t_r = 120$. Therefore, Λ_x increases faster than Λ_z, suggesting that the velocity field becomes more anisotropic with time in the WSL. The wavelengths Λ_x and Λ_z are related to the longitudinal and transverse integral scales of u, respectively. As discussed above, the length-scale ratio between the longitudinal and transverse integral scales is 2 in homogeneous isotropic turbulence. The faster growth of Λ_x compared with Λ_z results in an increase in Λ_x/Λ_z in the WSL, and the length-scale ratio in the WSL becomes much larger than the isotropic value of 2.

C. Proper orthogonal decomposition (POD)

The influence of the wall on the turbulent shear layer allows the growth of ELSS, which can be defined as energetic turbulent motions with a streamwise length much larger than the shear layer thickness.

The existence of ELSS is evident from the energy spectrum presented above. However, their various characteristics are not clear from the conventional statistics. Therefore, a proper orthogonal decomposition (POD) is employed to extract and analyze the velocity fluctuations associated with the ELSS. The POD is one of the most widely used tools for extracting energetic turbulent structures from a flow.[57–61] The detail of the POD analysis is presented in the Appendix. Here, the POD is applied to the instantaneous velocity vector on the x–z plane, $\mathbf{u}(x, y = 0, z) = (u, v, w)$, at a given time step, and $\mathbf{u}$ is decomposed into many modes. The first mode represents the mode that makes the largest contribution to the turbulent kinetic energy, and the modes are arranged in descending order of energy content.

Figure 16(a) presents the cumulative energy content, $F(N)$ in Eq. (A6), from the first to the Nth mode as a function of N while Fig. 16(b) shows the energy content of each mode (Nth mode from $N = 1$ to 51), which is also defined in the Appendix. The results are
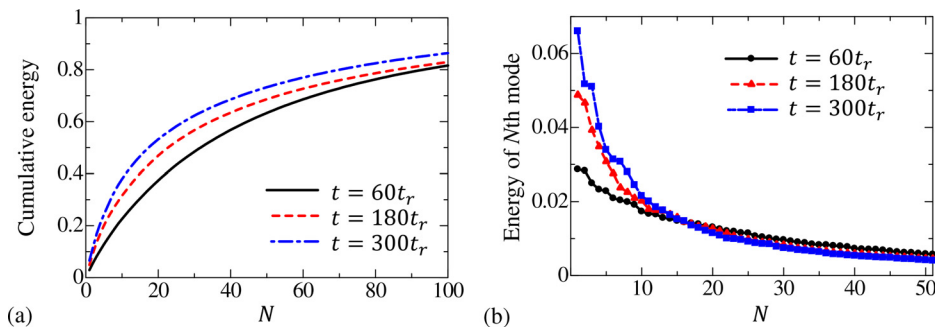

FIG. 16. POD analysis at the center of the WSL: (a) cumulative energy content with first N modes; (b) energy content of each mode N.
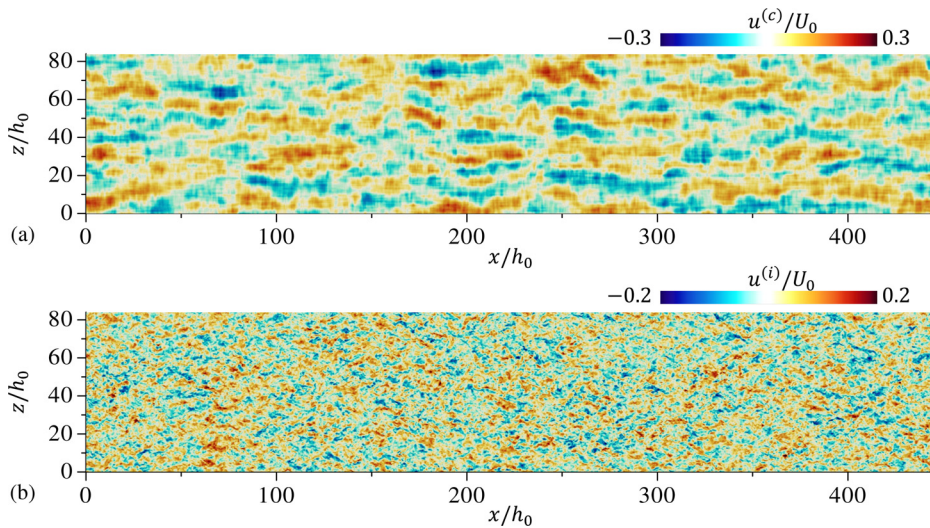
FIG. 17. Instantaneous streamwise velocity decomposed by the POD into (a) a coherent component $u^{(c)}$ and (b) an incoherent (remaining) component $u^{(i)}$ at $t/t_r = 300$ in the WSL. The results are shown on the x–z plane at $y = 0$. Here, the coherent component contains 50% of the total energy ($\lambda_{\mathrm{th}} = 0.5$).

obtained at $t/t_r = 60$, 180, and 300 in the WSL. In Fig. 16(a), the cumulative energy increases rapidly from $N = 1$ to about 20. At $t/t_r = 300$, 50% of the energy is possessed by 18 modes. A comparison between different time instances in Fig. 16(b) suggests that the energy content for $N \lesssim 15$ and $N \gtrsim 15$ increases and decreases with time, respectively. Thus, a large amount of the energy is occupied by fewer modes at a later time. This suggests that energetic flow structures are described by a small number of modes after the ELSS grows.

The velocity field is decomposed with the POD into two components. Here, a coherent component $\mathbf{u}^{(c)}$ is defined as the velocity consisting of the POD modes from $N = 1$ to $N_{\mathrm{th}}(\lambda_{\mathrm{th}})$, where $N_{\mathrm{th}}(\lambda_{\mathrm{th}})$ indicates that $100\lambda_{\mathrm{th}}$ % of the total energy is contained in the first to the $N_{\mathrm{th}}(\lambda_{\mathrm{th}})$ th modes. A similar decomposition with the threshold of cumulative energy has been widely applied in previous studies.[46,62] The remaining mode corresponds to an incoherent component $\mathbf{u}^{(i)} = \mathbf{u} - \mathbf{u}^{(c)}$. Here, we use "incoherent" simply as a counterpart of "coherent" and do not intend to claim that $\mathbf{u}^{(i)}$ is structureless. Most results presented below are obtained with $\lambda_{\mathrm{th}} \approx 0.5$ because the results are not qualitatively sensitive to a small change in λ_{th}.

Figure 17 visualizes $u^{(c)}$ and $u^{(i)}$ on the center plane of the WSL at $t/t_r = 300$. The velocity fluctuations with large streamwise length scales are captured well by the $u^{(c)}$ extracted by the POD. The remaining component $u^{(i)}$ has a smaller characteristic length scale than $u^{(c)}$. These results suggest that the POD is useful to extract the ELSS developing in turbulent shear layers.

Figure 18 shows the streamwise-wavenumber spectra of u, $u^{(c)}$, and $u^{(i)}$, which are denoted by $E_u(k_x)$, $E_u^{(c)}(k_x)$, and $E_u^{(i)}(k_x)$, respectively. The POD results are compared between different thresholds λ_{th}. The peak of $k_x E_u$ at $\lambda_x/\delta_u \approx 7$ is observed for E_u and $E_u^{(c)}$, while $E_u^{(i)}$ at this wavelength is small. Thus, the velocity fluctuations of ELSS are successfully extracted by the POD. On the other hand, $E_u^{(i)}$ peaks at $\lambda_x/\delta_u \approx 10^0$. One of the characteristic length scales of large-scale motions in the turbulent shear layer is δ_u. Therefore, turbulent motions at this length are expressed by the POD modes corresponding to $\mathbf{u}^{(i)}$. At still smaller scales, $E_u^{(i)}$ is close to E_u, and small-scale fluctuations are dominated by $\mathbf{u}^{(i)}$.

The Reynolds stress $\overline{u'v'}$ can also be decomposed with $u' = u'^{(c)} + u'^{(i)}$ and $v' = v'^{(c)} + v'^{(i)}$ as $\overline{u'v'} = \overline{u'^{(c)}v'^{(c)}} + \overline{u'^{(i)}v'^{(i)}}$ because of the orthogonality of the decomposition. The scale dependence of the Reynolds stress is examined with the cospectra of (u', v'), $(u'^{(c)}, v'^{(c)})$, and $(u'^{(i)}, v'^{(i)})$, which are denoted by C_{uv}, $C_{uv}^{(c)}$, and $C_{uv}^{(i)}$, respectively. Figure 19 compares $k_x C_{uv}(k_x)$, $k_x C_{uv}^{(c)}(k_x)$, and $k_x C_{uv}^{(i)}(k_x)$ at $t/t_r = 80$ and 300. In the turbulent shear layer, negative $\overline{u'v'}$ contributes to the production of turbulent kinetic energy. Negative peaks of $k_x C_{uv}$ and $k_x C_{uv}^{(c)}$ appear at $\lambda_x/\delta_u \approx 2$ for $t/t_r = 80$ and at $\lambda_x/\delta_u \approx 7$ for $t/t_r = 300$. Thus, the turbulent kinetic energy production at late times is dominated by the velocity fluctuations of the ELSS with $\lambda_x/\delta_u \gg 1$. The energy production by the ELSS is captured well by the coherent component extracted by the POD. On the other hand, $k_x C_{uv}^{(i)}$ has a negative peak at $\lambda_x/\delta_u \approx 1$, while this peak is smaller than that of $k_x C_{uv}^{(c)}$. The cospectrum becomes positive for $0.1 \lesssim \lambda_x/\delta_u \lesssim 0.2$ at $t/t_r = 300$, while positive $k_x C_{uv}^{(i)}$ is not noticeable at $t/t_r = 80$. The integral of C_{uv} is equal to $\overline{u'v'}$, which is the vertical turbulent flux of streamwise momentum. Positive $k_x C_{uv}^{(i)}$ at small scales indicates that
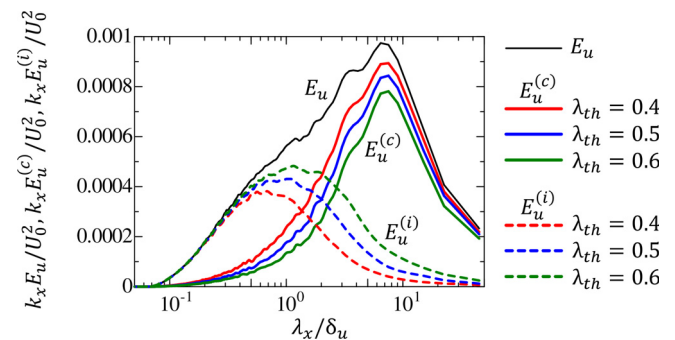

FIG. 18. Premultiplied energy spectra of streamwise velocity decomposed by the POD at $y = 0$ and $t/t_r = 300$ in the WSL. E_u, $E_u^{(c)}$, and $E_u^{(i)}$ are the energy spectra of u, $u^{(c)}$, and $u^{(i)}$, respectively. The spectra obtained with different thresholds λ_{th} of the POD are shown to examine the threshold dependence.
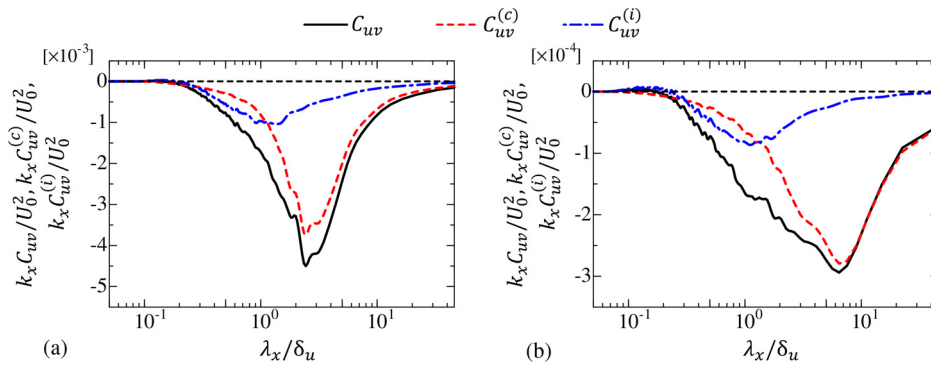
FIG. 19. Premultiplied cospectrum of streamwise and vertical velocity fluctuations $k_x C_{uv}$ at $y = 0$: (a) $t/t_r = 80$; (b) $t/t_r = 300$. The cospectra decomposed by the POD, $C_{uv}^{(c)}$ and $C_{uv}^{(i)}$, are also shown for comparison ($\lambda_{\text{th}} = 0.5$).

the momentum transport occurs in the counter-gradient direction. Similar counter-gradient momentum transport at small scales has also been reported in channel flows and stably stratified turbulent shear layers,[24,31] where the wavenumber dependence of $k_x C_{uv}$ is qualitatively similar to that in the WSL.

　　The effects of ELSS on the large-scale isotropy of the flow are investigated with the POD. Large-scale isotropy in turbulent flows is often evaluated with the normalized anisotropy tensor

$$b_{ij} = \frac{R_{ij}}{R_{kk}} - \frac{1}{3}\delta_{ij}, \qquad (8)$$

where $R_{ij} = \overline{u'_i u'_j}$ is the Reynolds stress tensor. The invariants of b_{ij} are defined as $\eta_b = (b_{ij}b_{ji}/6)^{1/2}$ and $\xi_b = (b_{ij}b_{jk}b_{ki}/6)^{1/3}$. Plots of (ξ_b, η_b) are often called the Lumley triangle, which is used to investigate the degree of anisotropy of R_{ij}.[51] We consider (ξ_b, η_b) defined with the Reynolds stress tensor decomposed by the POD as $R_{ij}^{(c)} = \overline{u'^{(c)}_i u'^{(c)}_j}$ and $R_{ij}^{(i)} = \overline{u'^{(i)}_i u'^{(i)}_j}$. Figure 20 presents the trajectory of (ξ_b, η_b) from $t/t_r = 100$ to 340 at $y = 0$. The present results are compared with numerical simulations of a freely developing turbulent shear layer[46] and a SSSL.[24] The three dashed lines represent special states of R_{ij}.[51] An axisymmetric state with one large eigenvalue is expressed by $\eta_b = \xi_b$. This relation is observed for the Reynolds stress in turbulent boundary layers except for viscous sublayers. Another axisymmetric state with one small eigenvalue is given by $\eta_b = -\xi_b$. An example of turbulent flows with $\eta_b = -\xi_b$ is a turbulent mixing layer.

The curve that connects the lines of $\eta_b = \xi_b$ and $\eta_b = -\xi_b$ is given by $\eta_b = (1/27 + 2\xi_b^3)^{1/2}$, which corresponds to a two-dimensional state of R_{ij}. This relation is found in the viscous sublayers of wall turbulence. R_{ij} hardly varies with flow development in the freely developing turbulent shear layer, for which (ξ_b, η_b) taken at a specific streamwise location is plotted in the figure. On the other hand, (ξ_b, η_b) varies with time in the temporally developing SSSL. Therefore, (ξ_b, η_b) from $t/t_r = 100$ to 340 is plotted for this flow. The WSL reaches the walls at $t/t_r \approx 100$, and the flow development is influenced by the walls for $t/t_r \gtrsim 100$. At $t/t_r = 100$, (ξ_b, η_b) defined with R_{ij} in the WSL is close to the line $\eta_b = -\xi_b$ and the data of the freely developing turbulent shear layer. However, ξ_b increases with time, and (ξ_b, η_b) approaches $\eta_b = \xi_b$. The plot of (ξ_b, η_b) for R_{ij} at $t/t_r = 180$ is close to that of the SSSL. Thus, the degree of isotropy changes when the shear layer development is confined by the walls. For the Reynolds stress decomposed by the POD, (ξ_b, η_b) of $R_{ij}^{(i)}$ hardly depends on time and is close to the isotropic state with $(\xi_b, \eta_b) = (0, 0)$. Therefore, the temporal variation of (ξ_b, η_b) of R_{ij} is attributed to that of $R_{ij}^{(c)}$, for which (ξ_b, η_b) is also shifted from $\eta_b = -\xi_b$ toward $\eta_b = \xi_b$.

D. Comparison of FSL, WSL, and SSSL

　　Comparisons of the FSL and WSL confirm that anisotropic velocity fluctuations grow in the turbulent shear layer confined by horizontal walls. The horizontal scale of the velocity fluctuations becomes much larger than the vertical length scale defined with the shear layer
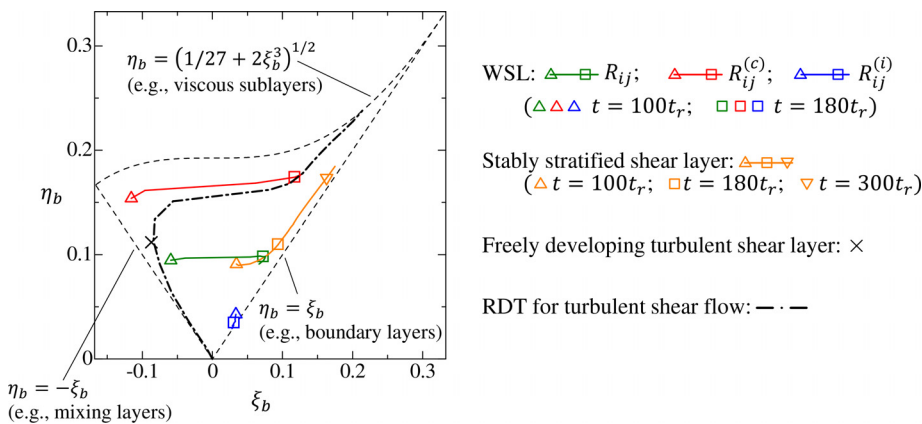

FIG. 20. Temporal variations of ξ_b and η_b at $y = 0$ from $t/t_r = 100$ to 340 in the WSL. The invariants (ξ_b, η_b) of Eq. (8) are evaluated with R_{ij}, $R_{ij}^{(c)}$, and $R_{ij}^{(i)}$, for which the POD is used with $\lambda_{\text{th}} = 0.5$. FIG also shows data of DNS for a freely developing turbulent shear layer,[46] LES for a SSSL,[24] and rapid distortion theory (RDT) for initially isotropic turbulence subject to simple shear.[51] The results for the SSSL are shown for $100 \le t/t_r \le 340$. The three dashed lines correspond to an axisymmetric state with one large eigenvalue $\eta_b = \xi_b$ or one small eigenvalue $\eta_b = -\xi_b$ and to a two-dimensional state $\eta_b = (1/27 + 2\xi_b^3)^{1/2}$.

thickness. Interestingly, the flow development of the WSL observed in this study is qualitatively similar to that of a stably stratified turbulent shear layer[15,17,19,63–69] in many aspects, as discussed below.

The stably stratified turbulent shear layer develops under the influence of the buoyancy force, which generally suppresses the vertical motions at large scales. The WSL is compared with LES results for a SSSL at $Re = 2000$ and $Ri = 0.06$,[24] where Ri is the Richardson number defined with the initial profiles of velocity and density. The size of the computational domain, the number of grid points, the initial conditions, and the Reynolds number of the LES are the same as those used for the FSL in this study. The differences are in the governing equations, which are the Navier–Stokes equations with the Boussinesq approximation for the SSSL. Figure 9 compares the shear layer thickness δ_u between the WSL and the SSSL. Until $t/t_r \approx 150$, δ_u in the stratified shear layer increases rapidly with time because of turbulent mixing caused by the instability. However, δ_u does not grow to be greater than about $9h_0$. The thickness of the WSL also cannot be larger than $10h_0$, because of the wall confinement. In the stratified shear layer, the layer growth is inhibited by the suppression of vertical motions by buoyancy. In both flows, the vertical length scale is fixed to be $\delta_u/h_0 \approx 10$, which hardly increases with time.

The growth of highly anisotropic velocity fluctuations is also observed in the SSSL. The wavelength Λ_x at which the energy spectrum $k_x E_u(k_x)$ reaches the local maximum is compared between the two flows in Fig. 15(a). As also found for the WSL, Λ_x normalized by δ_u increases with time in the SSSL, and the horizontal scale of large-scale velocity fluctuations becomes much larger than the vertical scale. This increase in the horizontal scale results in the emergence of ELSS

identified in the velocity profile on the horizontal plane. When the stratification effect is weak, the growth of the shear layer thickness continues even at a late time. In this case, ELSS are not observed in the flow, and the peak of the energy spectrum does not appear for $\Lambda_x/\delta_u \gg 1$.[24] The ELSS in the WSL and the SSSL are generated when the growth of δ_u is inhibited by the walls or by buoyancy. Therefore, this implies that the vertical confinement on the turbulent shear layer is related to the growth of ELSS.

In Fig. 20, (ξ_b, η_b) of the WSL and the SSSL appear near the line $\eta_b = \xi_b$, for which the Reynolds stress tensor is in an axisymmetric state with one large eigenvalue. However, (ξ_b, η_b) in these flows is very different from that in the freely developing turbulent shear layer. These comparisons also suggest that the vertical confinement by the walls in the WSL and the buoyancy in the SSSL have a qualitatively similar influence on the isotropy of the Reynolds stress. One noticeable difference in (ξ_b, η_b) between these flows is in its long-time evolution: $(\xi_b, \eta_b) \approx (0.07, 0.1)$ hardly varies after $t/t_r = 180$ in the WSL, while ξ_b and η_b increase along the line $\eta_b = \xi_b$ in the SSSL. The stable stratification results in a faster decay of R_{ij} in the SSSL than in the WSL. This difference can be related to different values of (ξ_b, η_b) at large t, although both flows have $\xi_b \approx \eta_b$.

Figure 21(a) visualizes the instantaneous streamwise velocity u on the horizontal plane at the center of the SSSL.[24] Here, the POD used for the WSL in Fig. 17 is applied to the velocity field in the SSSL. The coherent and incoherent components of u are visualized in Figs. 21(b) and 21(c), respectively. The velocity profile of $u^{(c)}$ is similar to that in the WSL shown in Fig. 17(a), and the large-scale velocity field is dominated by the anisotropic flow structures, whose streamwise length is much
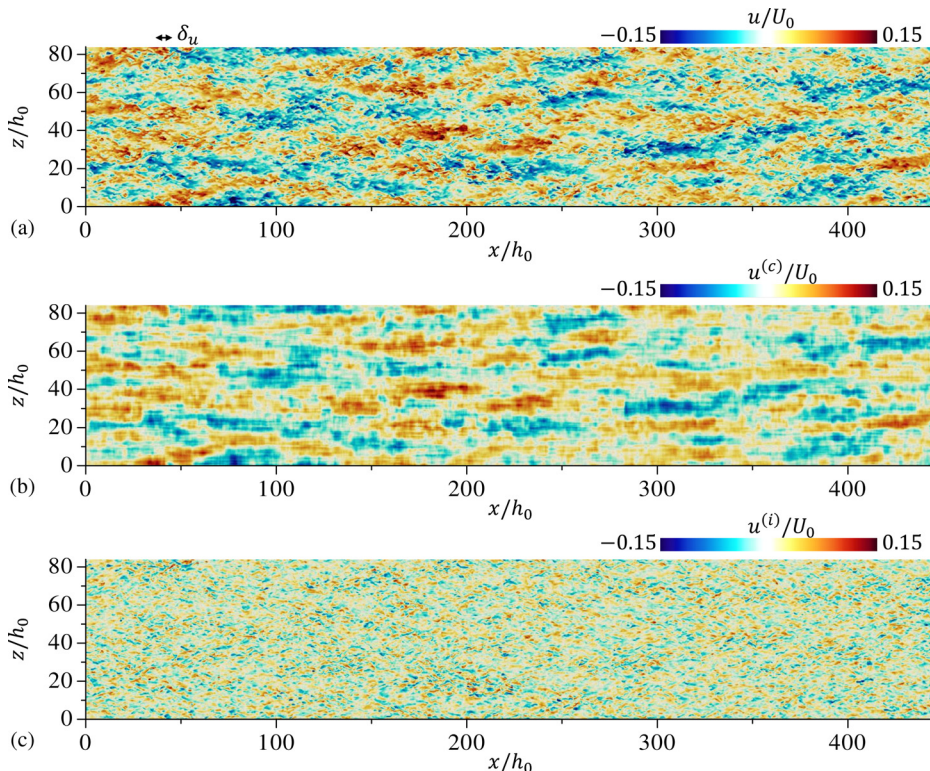

FIG. 21. POD analysis of the instantaneous streamwise velocity profile on the horizontal center plane of a SSSL at $t/t_r = 300$: (a) instantaneous streamwise velocity u; (b) coherent component $u^{(c)}$; (c) incoherent component $u^{(i)}$. Here, the coherent component contains 50% of the total energy ($\lambda_{th} = 0.5$).

larger than the length scales in the other directions. Thus, the POD is going to be a useful tool to investigate ELSS in SSSLs.

E. Effects of mean shear on the development of ELSS

A possible reason for the growth of ELSS in the WSL and SSSL is a high shear rate in these flows as also pointed out for the SSSL in Ref. 21. One of the dominant parameters of turbulent shear flows is a timescale ratio between mean shear and large-scale turbulent motions.[70–72] This ratio is also called a shear parameter. We define a bulk shear timescale of the turbulent shear layer as $\tau_{S_B} = \delta_u/U_0$. This definition ignores the spatial distribution of mean shear, whose influence is discussed below. A characteristic timescale of large-scale turbulent motions can be defined as $\tau_L = \Lambda_x/q$ with a velocity scale $q = \sqrt{u_{\mathrm{rms}}^2 + v_{\mathrm{rms}}^2 + w_{\mathrm{rms}}^2}$ and the peak wavelength of $k_x E_u(k_x)$, Λ_x. A bulk shear parameter is defined as $S_B^* = \tau_L/\tau_{S_B}$. Large values of S_B^* indicate strong influences of the mean shear on large-scale turbulent motions. Figure 22(a) shows the temporal evolutions of τ_{S_B} and τ_L, the latter of which is evaluated at the center of the shear layers. In most turbulent flows, the length scales of velocity fluctuations increase as the flow evolves. This is confirmed by the increase in Λ_x in the WSL and FSL in Fig. 15. As also shown in Figs. 5 and 6, q slowly decays in the WSL while it hardly varies with time in the FSL. Therefore, τ_L increases with time in both flows. The temporal evolution of τ_L is also similar in the SSSL, where Λ_x and q become large and small with time, respectively.[24] The bulk shear timescale τ_{S_B} varies differently between the WSL and FSL. As the shear layer thickness δ_u monotonically increases in the FSL, τ_{S_B} increases with time. However, τ_{S_B} in the WSL hardly varies with time after $t/t_r \approx 100$ because the growth of δ_u is inhibited by the walls. The stably stratification also results in almost constant τ_{S_B} for the same reason. Figure 22(b) compares the temporal evolution of S_B^* in the WSL, FSL, and SSSL. Because of the continuous growth of τ_{S_B} in the FSL, the FSL has smaller S_B^* than the WSL and SSSL, after $t/t_r \approx 100$. Large S_B^* in the WSL and SSSL indicates strong influences of the mean shear on the flow development at large scales, compared with the FSL.

The mean shear causes deformation of fluid element, whose influence on turbulence is often studied with rapid distortion theory (RDT).[73] The RDT relies on linearized Navier–Stokes equations and has been applied to elucidate the effects of mean shear on turbulent flows.[74] Lee *et al.*[75] investigated homogeneous turbulent flows subject to mean shear with DNS and RDT, which explain well the behaviors

of the WSL and SSSL as discussed here. Their visualization with DNS indicates that elongated structures with streaky velocity patterns are generated for a high shear rate, i.e., a large shear parameter, while they are absent for a low shear rate. The RDT has also predicted the generation of similar streaky structures at a large shear parameter. Their comparison between the DNS and RDT suggests that the deformation by shear, described by the linear theory, is essential for the formation of the streaky structures. Consistently, both DNS and RDT indicate that the longitudinal integral length scale of streamwise velocity monotonically increases with time under the influence of strong shear. The length scale ratio between the streamwise and spanwise integral scales also increases with time if the shear rate is high, implying that large-scale structures are elongated in the streamwise direction and become anisotropic by the mean shear effects. The different behaviors of the WSL, FSL, and SSSL are well explained with the dependence on the shear parameter observed in the DNS and RDT of turbulent shear flows. The streaky patterns of the ELSS are found in the WSL and SSSL with large S_B^* while the ELSS are absent in the FSL with small S_B^* (Figs. 10, 11, and 21). As expected from the RDT, the strong shear effects in the WSL and SSSL can also cause an increase in the streamwise length scale, which becomes much larger than the scales in the other directions (Fig. 15).

The RDT has also been used to examine the response of initially isotropic turbulence which is suddenly subject to rapid distortion.[51,76] Figure 20 includes (ξ_b, η_b) obtained by a numerical analysis with the RDT for the case of simple shear.[51] Isotropic turbulence has $(\xi_b, \eta_b) = (0, 0)$, which is the initial condition of the analysis. Once the flow is subject to the shear, the flow evolves on the plane of (ξ_b, η_b) to the upper left of the triangle along the line of $\eta_b = -\xi_b$. Then, ξ_b increases toward $\xi_b > 0$. The trajectory from negative to positive ξ_b is similar in the RDT and the coherent component $R_{ij}^{(c)}$, which is related to the ELSS in the WSL. Thus, the isotropy state of the WSL behaves similarly to the solution of the RDT. The Richardson-number (Ri) dependence of the development of ELSS has been investigated for the SSSL in Ref. 24. The ELSS does not develop in the SSSL when Ri is not large enough to suppress the growth of δ_u. In this case, the shear timescale τ_{S_B} monotonically increases as also observed for the FSL in Fig. 22(a). DNS and RDT of homogeneous shear flow also suggest that elongated flow structures do not appear when the mean shear is not strong.[75] Thus, the absence of the ELSS for low Ri cases is explained by
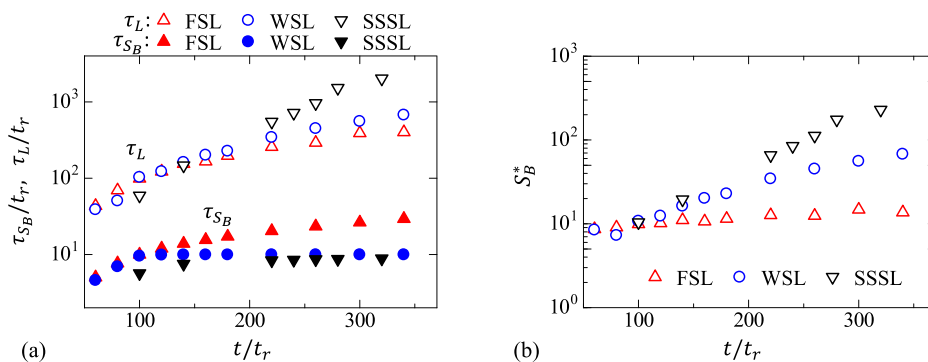

(a)   (b)

FIG. 22. Temporal evolutions of (a) the bulk shear timescale τ_{S_B} and timescale of large-scale turbulent motions τ_L and (b) the bulk shear parameter S_B^*. Here, τ_L is evaluated at $y = 0$. The results for the SSSL are also shown for comparison.[24]
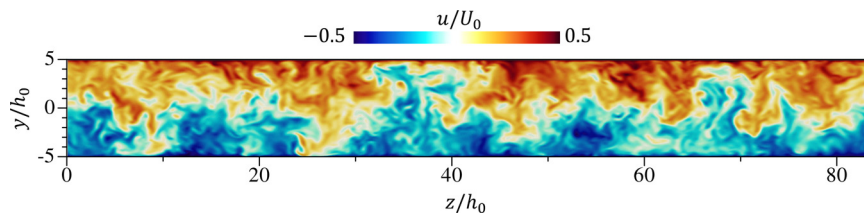
FIG. 23. Instantaneous streamwise velocity u on a y–z plane in the WSL at $t/t_r = 180$.

the relatively weak shear with a small shear parameter. These comparisons with RDT suggest that the evolution of large-scale turbulent motions in the WSL and SSSL is dominated by the deformation due to mean shear.

The spatial profile of the mean shear is different in the WSL and SSSL even though they have large values of the bulk shear parameter. The mean velocity profile of the SSSL is similar to that of the FSL and the mean shear is the strongest at the center of the shear layer.[24] However, Fig. 6(a) shows that the shear in the WSL becomes strong away from the centerline after the walls begin to suppress the shear layer growth. This tendency is more prominent at a later time, and the strong shear is concentrated for $|y|/H \gtrsim 0.4$. Despite the weaker mean shear near the center of the WSL, the ELSS appears at all vertical locations. Figure 23 visualizes the instantaneous streamwise velocity profile on a y–z plane at $t/t_r = 180$ for the WSL. The ELSS is developing at this time as confirmed by the increase in the peak wavelength in Fig. 15(a). The distribution of regions with $u > 0$ and $u < 0$ indicates that the velocity profile has a correlation between the center and the near-wall region of the shear layer and implies that the vertical size of the ELSS is of the order of the shear layer thickness δ_u. The large-scale turbulent motions in the shear layer are strongly deformed by the mean shear in the near-wall region. However, this influence can prevail at the center of the shear layer because the vertical length scale of turbulence is about δ_u. This is also explained by the cospectrum of u and v in Fig. 19, which indicates active turbulent mixing in the vertical direction at the length scales of ELSS: a fluid parcel that is significantly deformed by the shear near the walls can be advected toward the center of the shear layer. This is contrary to the ELSS in the SSSL, in which the vertical turbulent mixing associated with the ELSS is not significant.[24] The strong influence of mean shear is observed near the center of the SSSL, where the ELSS develops due to the large mean velocity gradient, while the ELSS is absent near the edge of the SSSL because the ELSS generated at the center is hardly advected in the vertical direction. Therefore, the stable stratification significantly affects the vertical distribution of the ELSS.

The ELSS has been observed in the SSSL where the density gradient is locally large inside the shear layer and the ambient fluid has a constant density.[21,24] SSSLs in a uniformly stratified fluid have also been studied in previous studies.[19,63,69,77,78] When a shear layer develops in a uniformly stratified fluid, internal gravity waves are excited outside the shear layer. Previous DNS studies of the SSSLs with uniform stratification have used small computational domains which cannot contain the ELSS. Therefore, it is not clear if the ELSS also develops in SSSLs with uniform stratification. The SSSLs with these density distributions were compared in Refs. 19 and 69. For a certain range of an initial Richardson number, a long-time behavior of δ_u is similar for both density profiles. The above discussion suggests that the suppression of the increase in δ_u is a key for the development of

ELSS. Therefore, it is implied that the ELSS may also develop in SSSLs with uniform stratification when the stratification is strong enough to suppress the increase in δ_u and weak enough for the shear instability to generate turbulence. DNS or LES with a very large computational domain will be useful to clarify the existence of ELSS in a uniformly stratified fluid in future studies.

IV. CONCLUSION

Large-eddy simulations (LES) have been performed for a freely developing shear layer (FSL) and for a wall-confined shear layer (WSL) that develops between two horizontal walls. Both flows become turbulent as a result of shear instability and develop in the vertical direction. The shear layer thickness δ_u in the FSL increases continuously with time. However, δ_u in the WSL cannot grow larger than the distance between the walls. The effect of wall confinement on the turbulent shear layer has been investigated by comparing these flows.

Highly anisotropic velocity fluctuations are generated after the confinement effect begins to prevent the growth of the shear layer thickness in the WSL. In the velocity field, these velocity fluctuations are recognized as elongated large-scale structures (ELSS), whose streamwise length scales are much larger than the scales in the other directions, such as the shear layer thickness and the spanwise length of ELSS. The emergence of ELSS also affects the shape of the energy spectrum. The premultiplied energy spectrum $k_x E_u$ peaks at an energy-containing length scale. The peak wavelengths in the streamwise and spanwise directions (Λ_x and Λ_z, respectively) normalized by δ_u do not vary with time in the FSL. Therefore, the length-scale ratios of large-scale velocity fluctuations, Λ_x/δ_u and Λ_x/Λ_z, are almost constant in the FSL. However, Λ_x/δ_u increases with time in the WSL, indicating that the streamwise length scale becomes much larger than the vertical length scale. Although Λ_z also slowly increases in the WSL, the streamwise length scale becomes much larger than the spanwise scale because of the different growth rates of Λ_x and Λ_z.

The present LES results also suggest that a proper orthogonal decomposition (POD) is useful to extract the velocity fluctuations associated with the ELSS. POD analysis shows that the ELSS dominate the vertical momentum transport in the WSL. The isotropy of the Reynolds stress tensor R_{ij} has been evaluated by the Lumley triangle, calculated using the velocity components decomposed by the POD. Before the ELSS develop, the state of the isotropy is similar between the WSL and the freely developing turbulent shear layer. The Reynolds stress related to the ELSS is as anisotropic as the SSSL. The emergence of the ELSS changes the overall isotropy of R_{ij}, because the ELSS make a dominant contribution to the Reynolds stress and the turbulent kinetic energy.

These behaviors of the WSL are consistent with those of stably stratified turbulent shear layers with moderately large Richardson

numbers. We have compared the flow development between the WSL and a SSSL.[21,24] Because of the suppression of vertical turbulent motions by buoyancy, the thickness of the SSSL hardly grows with time. The wall confinement in the WSL has a similar effect on the growth of the layer thickness. In both flows, anisotropic velocity fluctuations of ELSS are generated after the shear layer thickness becomes almost constant. Consequently, an increase in Λ_x due to the growth of the ELSS is observed in the WSL and the SSSL.

The temporal evolution of the bulk shear parameter suggests that the effects of mean shear become significant when the growth of the shear layer thickness is inhibited in the WSL and SSSL. The flow behavior in these flows is qualitatively consistent with DNS and RDT for homogeneous shear flows,[51,75] which indicate that elongated flow structures with streaky patterns are formed when the turbulent flow is subject to strong mean shear. Consequently, the streamwise integral scale becomes greater than the spanwise one by deformation due to the shear. The change of the isotropy state on the Lumley triangle associated with the ELSS also agrees with the flow response to the mean shear predicted by the RDT. These comparisons suggest the strong mean shear is a key to the formation of ELSS in the WSL and SSSL. The spatial distribution of mean shear is different between the WSL and SSSL. The WSL has stronger mean shear away from the center of the shear layer. However, the vertical scale of large-scale velocity fluctuations is as large as the shear layer thickness and the vertical turbulent mixing is active at the large scales. Therefore, the mean shear away from the center can affect the flow structures in the entire flow field, and the ELSS is still observed at the center of the WSL. On the other hand, the SSSL has the strongest mean shear at the center and the vertical turbulent mixing is not active at the streamwise scale of the ELSS. This explains why the ELSS is observed only near the center of the SSSL.[24] Thus, the stable stratification is related to different vertical distributions of the ELSS in these flows. These comparisons suggest that the vertical confinement of the shear layer results in the strong mean shear effects, which cause the development of anisotropic velocity fluctuations with very large streamwise length scales. The confinement effects arise from different physical mechanisms in the WSL and SSSL, implying that the flow behavior related to the ELSS can be universal for turbulent shear layers with a fixed vertical length scale.

AUTHOR DECLARATIONS
Conflict of Interest

The authors have no conflicts to disclose.

DATA AVAILABILITY

The data that support the findings of this study are available from the corresponding author upon reasonable request.

APPENDIX: PROPER ORTHOGONAL DECOMPOSITION

This appendix describes the procedure to apply the proper orthogonal decomposition (POD) to horizontal profiles of velocity vectors. A snapshot POD is often applied to time series data of fluctuating components of flow variables when a flow is statistically stationary and the fluctuations are defined with time averages.[57,58,61,79] The temporally developing turbulent shear layers are statistically homogeneous in the streamwise (x) and spanwise (z) directions and are not statistically stationary. Therefore, the POD is applied to fluctuations from a spatial average, which is evaluated with the average in the x direction as explained below. The procedure given here can be derived by replacing t in that for statistically stationary flows with x. In this appendix, the summation rule for repeated indices is not applied and is explicitly written with Σ. In addition, vector quantities are expressed with bold italic (e.g., $\boldsymbol{q}$ and $\boldsymbol{\phi}$) while bold-sloping sans serif is used for matrices (e.g., R). Components of vectors and matrices are written with light italic with subscripts (e.g., ϕ_i and R_{ij}).

We consider a flow field at given time and vertical location $(t, y) = (t_0, y_0)$, for which variables are expressed as functions of (x, z). The profile of velocity vectors is written as (u_{ki}, v_{ki}, w_{ki}), where the integers, $k = 1, \ldots, N_z$ and $i = 1, \ldots, N_x$, represent the grid location in the z and x directions, respectively. An average of f_{ki} is taken in the x direction on the plane of $y = y_0$ and is given as a function of z by $\tilde{f}_k = (1/N_x) \sum_{i=1}^{N_x} f_{ki}$. Fluctuating velocity vectors are defined as $(u'_{ki}, v'_{ki}, w'_{ki}) = (u_{ki} - \tilde{u}_k, v_{ki} - \tilde{v}_k, w_{ki} - \tilde{w}_k)$, which are rearranged in the following matrix form:

$$
\boldsymbol{Q} = \begin{pmatrix}
u'_{11} & \cdots & u'_{1i} & \cdots & u'_{1N_x} \\
\vdots & \ddots & & & \vdots \\
u'_{k1} & & u'_{ki} & & u'_{kN_x} \\
\vdots & & & \ddots & \vdots \\
u'_{N_z 1} & \cdots & u'_{N_z i} & \cdots & u'_{N_z N_x} \\
v'_{11} & \cdots & v'_{1i} & \cdots & v'_{1N_x} \\
\vdots & \ddots & & & \vdots \\
v'_{k1} & & v'_{ki} & & v'_{kN_x} \\
\vdots & & & \ddots & \vdots \\
v'_{N_z 1} & \cdots & v'_{N_z i} & \cdots & v'_{N_z N_x} \\
w'_{11} & \cdots & w'_{1i} & \cdots & w'_{1N_x} \\
\vdots & \ddots & & & \vdots \\
w'_{k1} & & w'_{ki} & & w'_{kN_x} \\
\vdots & & & \ddots & \vdots \\
w'_{N_z 1} & \cdots & w'_{N_z i} & \cdots & w'_{N_z N_x}
\end{pmatrix} \in \mathbb{R}^{3N_z \times N_x}. \quad (A1)
$$

This matrix is also written with the combination of vectors $\boldsymbol{q}_i = (u_{1i}, \ldots, u_{N_z i}, v_{1i}, \ldots, v_{N_z i}, w_{1i}, \ldots, w_{N_z i})^T$ with $i = 1, \ldots, N_x$ as

$$
\boldsymbol{Q} = \begin{pmatrix} \boldsymbol{q}_1 & \cdots & \boldsymbol{q}_i & \cdots & \boldsymbol{q}_{N_x} \end{pmatrix}. \quad (A2)
$$

The POD applies the following decomposition of q_i:

$$q_i = \sum_{n=1}^{N_{\mathrm{mod}}} a_i^{(n)} \phi^{(n)}, \tag{A3}$$

where $N_{\mathrm{mod}} = N_x$ is the number of modes, $\phi^{(n)}$ is the nth-mode vector, and $a_i^{(n)}$ is the coefficient for the nth mode, which depends on $i = 1, \ldots, N_x$. A component of $\phi^{(n)} \in \mathbb{R}^{3N_z}$ is denoted by $\phi_m^{(n)}$ with $m = 1, \ldots, 3N_z$. In practice, $\phi_m^{(n)}$ and $a_i^{(n)}$ can be obtained from the eigenvalues $\lambda^{(n)}$ and eigenvectors $\psi^{(n)} \in \mathbb{R}^{N_x}$ of R, which is defined as $R = Q^T Q \in \mathbb{R}^{N_x \times N_x}$, or equivalently as $R_{m_a m_b} = \sum_{i=1}^{3N_z} Q_{im_a} Q_{im_b}$ for $m_a, m_b = 1, \ldots, N_x$. Here, the eigenvalues are arranged in the descending order as $\lambda^{(1)} \geq \lambda^{(2)} \geq \ldots \geq \lambda^{(N_x)}$. In this study, $\lambda^{(n)}$ and $\psi^{(n)}$ are calculated from R with the eigs function of MATLAB. The coefficients and mode vectors, $a_i^{(n)}$ and $\phi^{(n)}$, in Eq. (A3) are calculated as

$$\phi^{(n)} = \frac{1}{\sqrt{\lambda^{(n)}}} Q \psi^{(n)} \quad \text{or} \quad \phi_m^{(n)} = \frac{1}{\sqrt{\lambda^{(n)}}} \sum_{m_b=1}^{N_x} Q_{mm_b} \psi_{m_b}^{(n)}$$

with $m = 1, \ldots, 3N_z$, $\tag{A4}$

$$a_i^{(n)} = q_i \cdot \phi^{(n)}. \tag{A5}$$

Velocity vectors for the nth mode are calculated as $q_i^{(n)} = a_i^{(n)} \phi^{(n)}$ for $i = 1, \ldots, N_x$. The fractional energy content of Nth mode is $\lambda^{(n)} / \sum_{n=1}^{N_{\mathrm{mod}}} \lambda^{(n)}$. The cumulative energy contained from the 1st to Nth mode is given by

$$F(N) = \frac{\sum_{n=1}^{N} \lambda^{(n)}}{\sum_{n=1}^{N_{\mathrm{mod}}} \lambda^{(n)}}. \tag{A6}$$

We define $N_{\mathrm{th}}(\lambda_{\mathrm{th}})$ as the minimum number of modes for which F exceeds a threshold λ_{th}. By specifying λ_{th}, the velocity vectors of coherent components are obtained from $q_i^{(c)}$ calculated as

$$q_i^{(c)} = \sum_{n=1}^{N_{\mathrm{th}}(\lambda_{\mathrm{th}})} q_i^{(n)} = \sum_{n=1}^{N_{\mathrm{th}}(\lambda_{\mathrm{th}})} a_i^{(n)} \phi^{(n)} \tag{A7}$$

for $i = 1, \ldots, N_x$. Then, the velocity vectors of incoherent components are obtained by subtracting the coherent velocity vectors from the full velocity vectors.

REFERENCES

[1] G. L. Brown and A. Roshko, "On density effects and large structure in turbulent mixing layers," J. Fluid Mech. **64**, 775 (1974).

[2] D. Zhang, J. Tan, and X. Yao, "Direct numerical simulation of spatially developing highly compressible mixing layer: Structural evolution and turbulent statistics," Phys. Fluids **31**, 036102 (2019).

[3] M. M. Rogers and R. D. Moser, "Direct simulation of a self-similar turbulent mixing layer," Phys. Fluids **6**, 903 (1994).

[4] E. Balaras, U. G. O. Piomelli, and J. M. Wallace, "Self-similar states in turbulent mixing layers," J. Fluid Mech. **446**, 1 (2001).

[5] Y. Ito, K. Nagata, Y. Sakai, and O. Terashima, "Momentum and mass transfer in developing liquid shear mixing layers," Exp. Therm. Fluid Sci. **51**, 28 (2013).

[6] W. A. McMullan and S. J. Garrett, "Initial condition effects on large scale structure in numerical simulations of plane mixing layers," Phys. Fluids **28**, 015111 (2016).

[7] X.-X. Fang, C.-B. Shen, M.-B. Sun, H.-B. Wang, and P. Wang, "Turbulent structures and mixing enhancement with lobed mixers in a supersonic mixing layer," Phys. Fluids **32**, 041701 (2020).

[8] R. Boukharfane, A. Er-raiy, M. Elkarii, and M. Parsani, "A direct numerical simulation study of skewed three-dimensional spatially evolving compressible mixing layer," Phys. Fluids **33**, 115114 (2021).

[9] U. Unnikrishnan, H. Huo, X. Wang, and V. Yang, "Subgrid scale modeling considerations for large eddy simulation of supercritical turbulent mixing and combustion," Phys. Fluids **33**, 075112 (2021).

[10] W. D. Smyth and J. N. Moum, "Ocean mixing by Kelvin-Helmholtz instability," Oceanography **25**, 140 (2012).

[11] J. H. Hecht, D. C. Fritts, L. J. Gelinas, R. J. Rudy, R. L. Walterscheid, and A. Z. Liu, "Kelvin-Helmholtz billow interactions and instabilities in the mesosphere over the Andes Lidar observatory: 1. Observations," J. Geophys. Res. Atmos. **126**, e2020JD033414, http://dx.doi.org/10.1029/2020JD033414 (2021).

[12] D. C. Fritts, S. A. Wieland, T. S. Lund, S. A. Thorpe, and J. H. Hecht, "Kelvin–Helmholtz billow interactions and instabilities in the mesosphere over the Andes Lidar observatory: 2. Modeling and interpretation," J. Geophys. Res. Atmos. **126**, e2020JD033412, http://dx.doi.org/10.1029/2020JD033412 (2021).

[13] S. A. Thorpe, "Experiments on instability and turbulence in a stratified shear flow," J. Fluid Mech. **61**, 731 (1973).

[14] I. P. D. De Silva, A. Brandt, L. J. Montenegro, and H. J. S. Fernando, "Gradient Richardson number measurements in a stratified shear layer," Dyn. Atmos. Oceans **30**, 47 (1999).

[15] W. D. Smyth and J. N. Moum, "Length scales of turbulence in stably stratified mixing layers," Phys. Fluids **12**, 1327 (2000).

[16] K. A. Brucker and S. Sarkar, "Evolution of an initially turbulent stratified shear layer," Phys. Fluids **19**, 105105 (2007).

[17] A. Mashayek and W. R. Peltier, "The 'zoo' of secondary instabilities precursor to stratified shear flow transition. Part 1. Shear aligned convection, pairing, and braid instabilities," J. Fluid Mech. **708**, 5 (2012).

[18] W. R. Peltier and C. P. Caulfield, "Mixing efficiency in stratified shear flows," Annu. Rev. Fluid Mech. **35**, 135 (2003).

[19] A. VanDine, H. T. Pham, and S. Sarkar, "Turbulent shear layers in a uniformly stratified background: DNS at high Reynolds number," J. Fluid Mech. **916**, A42 (2021).

[20] H. T. Pham, S. Sarkar, and K. B. Winters, "Intermittent patches of turbulence in a stratified medium with stable shear," J. Turbul. **13**, N20 (2012).

[21] T. Watanabe, J. J. Riley, K. Nagata, K. Matsuda, and R. Onishi, "Hairpin vortices and highly elongated flow structures in a stably stratified shear layer," J. Fluid Mech. **878**, 37 (2019).

[22] S.-J. Kang, M. Tanahashi, and T. Miyauchi, "Dynamics of fine scale eddy clusters in turbulent channel flows," J. Turbul. **8**, N52 (2007).

[23] T. Watanabe, Y. Sakai, K. Nagata, Y. Ito, and T. Hayase, "Turbulent mixing of passive scalar near turbulent and non-turbulent interface in mixing layers," Phys. Fluids **27**, 085109 (2015).

[24] T. Watanabe and K. Nagata, "Large-scale characteristics of a stably stratified turbulent shear layer," J. Fluid Mech. **927**, A27 (2021).

[25] X. Wu and P. Moin, "Direct numerical simulation of turbulence in a nominally zero-pressure-gradient flat-plate boundary layer," J. Fluid Mech. **630**, 5 (2009).

[26] N. Hutchins and I. Marusic, "Evidence of very long meandering features in the logarithmic region of turbulent boundary layers," J. Fluid Mech. **579**, 1 (2007).

[27] J. P. Monty, N. Hutchins, H. C. H. Ng, I. Marusic, and M. S. Chong, "A comparison of turbulent pipe, channel and boundary layer flows," J. Fluid Mech. **632**, 431 (2009).

[28] J. Ahn and H. J. Sung, "Relationship between streamwise and azimuthal length scales in a turbulent pipe flow," Phys. Fluids **29**, 105112 (2017).

[29] T. Tong, K. Bhatt, T. Tsuneyoshi, and Y. Tsuji, "Effect of large-scale structures on wall shear stress fluctuations in pipe flow," Phys. Rev. Fluids **5**, 104601 (2020).

[30] X. Chen, K. Iwano, Y. Sakai, and Y. Ito, "The meandering bend features of large-scale structures and the related coherent structures," Int. J. Heat Fluid Flow **93**, 108915 (2022).

[31] M. Lee and R. D. Moser, "Spectral analysis of the budget equation in turbulent channel flows at high Reynolds number," J. Fluid Mech. **860**, 886 (2019).

[32]P. A. Davidson, *Turbulence: An Introduction for Scientists and Engineers* (Oxford University Press, 2004).

[33]T. Guo, M. J. Rau, P. P. Vlachos, and S. V. Garimella, "Axisymmetric wall jet development in confined jet impingement," Phys. Fluids **29**, 025102 (2017).

[34]S. Dave, C. Anghan, S. Saincher, and J. Banerjee, "Direct numerical simulation of forced turbulent round jet: Effect of flow confinement and varicose excitation," Phys. Fluids **33**, 075108 (2021).

[35]R. J. Gathmann, M. Si-Ameur, and F. Mathey, "Numerical simulations of three-dimensional natural transition in the compressible confined shear layer," Phys. Fluids **5**, 2946 (1993).

[36]R. Sampath and S. R. Chakravarthy, "Proper orthogonal and dynamic mode decompositions of time-resolved PIV of confined backward-facing step flow," Exp. Fluids **55**, 1 (2014).

[37]G. P. Benham, A. A. Castrejon-Pita, I. J. Hewitt, C. P. Please, R. W. Style, and P. A. D. Bird, "Turbulent shear layers in confining channels," J. Turbul. **19**, 431 (2018).

[38]Y. Tian, W. Shi, F. Zhong, and J. Le, "Pilot hydrogen enhanced combustion in an ethylene-fueled scramjet combustor at Mach 4," Phys. Fluids **33**, 015105 (2021).

[39]M. Gampert, J. Boschung, F. Hennig, M. Gauding, and N. Peters, "The vorticity versus the scalar criterion for the detection of the turbulent/non-turbulent interface," J. Fluid Mech. **750**, 578 (2014).

[40]T. Watanabe, C. B. da Silva, Y. Sakai, K. Nagata, and T. Hayase, "Lagrangian properties of the entrainment across turbulent/non-turbulent interface layers," Phys. Fluids **28**, 031701 (2016).

[41]R. Jahanbakhshi, N. S. Vaghefi, and C. K. Madnia, "Baroclinic vorticity generation near the turbulent/non-turbulent interface in a compressible shear layer," Phys. Fluids **27**, 105105 (2015).

[42]T. Watanabe, X. Zhang, and K. Nagata, "Direct numerical simulation of incompressible turbulent boundary layers and planar jets at high Reynolds numbers initialized with implicit large eddy simulation," Comput. Fluids **194**, 104314 (2019).

[43]S. Tanaka, T. Watanabe, and K. Nagata, "Multi-particle model of coarse-grained scalar dissipation rate with volumetric tensor in turbulence," J. Comput. Phys. **389**, 128 (2019).

[44]Y. Morinishi, T. S. Lund, O. V. Vasilyev, and P. Moin, "Fully conservative higher order finite difference schemes for incompressible flow," J. Comput. Phys. **143**, 90 (1998).

[45]C. A. Kennedy and M. H. Carpenter, "Several new numerical methods for compressible shear-layer simulations," Appl. Numer. Math. **14**, 397 (1994).

[46]K. Takamure, Y. Ito, Y. Sakai, K. Iwano, and T. Hayase, "Momentum transport process in the quasi self-similar region of free shear mixing layer," Phys. Fluids **30**, 015109 (2018).

[47]M. Gampert, K. Kleinheinz, N. Peters, and H. Pitsch, "Experimental and numerical study of the scalar turbulent/non-turbulent interface layer in a jet flow," Flow, Turbul. Combust. **92**, 429 (2014).

[48]Y. Tai, T. Watanabe, and K. Nagata, "Implicit large eddy simulation of passive scalar transfer in compressible planar jet," Int. J. Numer. Methods Fluids **93**, 1183 (2021).

[49]J. H. Bell and R. D. Mehta, "Development of a two-stream mixing layer from tripped and untripped boundary layers," AIAA J. **28**, 2034 (1990).

[50]M. Tanahashi, S. Iwase, and T. Miyauchi, "Appearance and alignment with strain rate of coherent fine scale eddies in turbulent mixing layer," J. Turbul. **2**, 1 (2001).

[51]S. B. Pope, *Turbulent Flows* (Cambridge University Press, 2000).

[52]N. Tillmark, "Experiments on transition and turbulence in plane Couette flow," Ph.D. thesis (Department of Mechanics, Royal Institute of Technology, Stockholm, Sweden, 1998).

[53]T. Tsukahara, H. Kawamura, and K. Shingai, "DNS of turbulent Couette flow with emphasis on the large-scale structure in the core region," J. Turbul. **7**, N19 (2006).

[54]N. Li, E. Balaras, and J. M. Wallace, "Passive scalar transport in a turbulent mixing layer," Flow, Turbul. Combust. **85**, 1 (2010).

[55]K. C. Kim and R. J. Adrian, "Very large-scale motion in the outer layer," Phys. Fluids **11**, 417 (1999).

[56]M. Takahashi, K. Iwano, Y. Sakai, and Y. Ito, "Three-dimensional visualization of destruction events of turbulent momentum transfer in a plane jet," Phys. Fluids **31**, 105114 (2019).

[57]L. Sirovich, "Turbulence and the dynamics of coherent structures. I. Coherent structures," Q. Appl. Math. **45**, 561 (1987).

[58]L. Wu, K. Chen, and C. Zhan, "Snapshot pod analysis of transient flow in the pilot stage of a jet pipe servo valve," J. Turbul. **19**, 889 (2018).

[59]O. Terashima, Y. Sakai, and Y. Ito, "Measurement of fluctuating temperature and POD analysis of eigenmodes in a heated planar jet," Exp. Therm. Fluid Sci. **92**, 113 (2015).

[60]G. Riches, R. Martinuzzi, and C. Morton, "Proper orthogonal decomposition analysis of a circular cylinder undergoing vortex-induced vibrations," Phys. Fluids **30**, 105103 (2018).

[61]M. Karami, H. Hangan, L. Carassale, and H. Peerhossaini, "Coherent structures in tornado-like vortices," Phys. Fluids **31**, 085118 (2019).

[62]S. Y. Motlagh and S. Taghizadeh, "POD analysis of low Reynolds turbulent porous channel flow," Int. J. Heat Fluid Flow **61**, 665 (2016).

[63]E. J. Strang and H. J. S. Fernando, "Entrainment and mixing in stratified shear flows," J. Fluid Mech. **428**, 349 (2001).

[64]M. Rahmani, B. R. Seymour, and G. A. Lawrence, "The effect of Prandtl number on mixing in low Reynolds number Kelvin-Helmholtz billows," Phys. Fluids **28**, 054107 (2016).

[65]H. Salehipour, W. Peltier, and A. Mashayek, "Turbulent diapycnal mixing in stratified shear flows: The influence of Prandtl number on mixing efficiency and transition at high Reynolds number," J. Fluid Mech. **773**, 178 (2015).

[66]T. Watanabe, J. J. Riley, and K. Nagata, "Effects of stable stratification on turbulent/nonturbulent interfaces in turbulent mixing layers," Phys. Rev. Fluids **1**, 044301 (2016).

[67]T. Watanabe, J. J. Riley, and K. Nagata, "Turbulent entrainment across turbulent-nonturbulent interfaces in stably stratified mixing layers," Phys. Rev. Fluids **2**, 104803 (2017).

[68]A. K. Kaminski and W. D. Smyth, "Stratified shear instability in a field of pre-existing turbulence," J. Fluid Mech. **862**, 639 (2019).

[69]S. F. Lewin and C. P. Caulfield, "The influence of far field stratification on shear-induced turbulent mixing," J. Fluid Mech. **928**, A20 (2021).

[70]J. Schumacher, "Relation between shear parameter and Reynolds number in statistically stationary turbulent shear flows," Phys. Fluids **16**, 3094 (2004).

[71]J. C. Isaza and L. R. Collins, "On the asymptotic behaviour of large-scale turbulence in homogeneous shear flow," J. Fluid Mech. **637**, 213 (2009).

[72]A. Sekimoto, S. Dong, and J. Jiménez, "Direct numerical simulation of statistically stationary and homogeneous shear turbulence and its relation to other shear flows," Phys. Fluids **28**, 035101 (2016).

[73]J. C. R. Hunt and D. J. Carruthers, "Rapid distortion theory and the 'problems' of turbulence," J. Fluid Mech. **212**, 497 (1990).

[74]A. A. Townsend, "Entrainment and the structure of turbulent flow," J. Fluid Mech. **41**, 13 (1970).

[75]M. J. Lee, J. Kim, and P. Moin, "Structure of turbulence at high shear rate," J. Fluid Mech. **216**, 561 (1990).

[76]A. A. Townsend, *The Structure of Turbulent Shear Flow* (Cambridge University Press, 1976).

[77]H. T. Pham, S. Sarkar, and K. A. Brucker, "Dynamics of a stratified shear layer above a region of uniform stratification," J. Fluid Mech. **630**, 191 (2009).

[78]T. Watanabe, J. J. Riley, K. Nagata, R. Onishi, and K. Matsuda, "A localized turbulent mixing layer in a uniformly stratified environment," J. Fluid Mech. **849**, 245 (2018).

[79]K. Taira, S. L. Brunton, S. T. M. Dawson, C. W. Rowley, T. Colonius, B. J. McKeon, O. T. Schmidt, S. Gordeyev, V. Theofilis, and L. S. Ukeiley, "Modal analysis of fluid flows: An overview," AIAA J. **55**, 4013 (2017).